# QUANTIFYING GULLY EROSION IN WEST TENNESSEE USING HIGH RESOLUTION LIDAR DATA

A Thesis Presented for the
Master of Science
Degree
The University of Tennessee, Knoxville

John James McNelis

May 2016

# ACKNOWLEDGEMENTS

It has been a tremendous pleasure to pursue my master's degree in Geography at the University of Tennessee. I credit the effort and guidance of many faculty members, fellow students, and close friends for the great personal and academic growth I've experienced through this process. Pursuing my master's degree has undoubtedly been the most valuable experience of my life. Admittedly, you'd have to look long and hard to find an entering graduate student as naïve to the scientific process as I was upon entering. This endeavor has given me the skills necessary to conduct research effectively, and, more importantly, helped me discover the unrealized potential within myself.

I owe my deepest appreciation to my committee chair, Dr. Yingkui Li, whose passion for research is infectious and interest in his students' education genuine. His persistent encouragement gave me the confidence to enter the graduate program and to develop the skills and understanding necessary to succeed in my studies. Dr. Li is not only a wonderful educator and advisor, but a remarkably kind person to whom I owe immense gratitude.

I credit Dr. Robert Washington-Allen for fostering what is sure to be a lifelong passion for remote sensing. His enthusiasm inspires my own and through his instruction he has afforded me an understanding of the fundamentals in ways that allow me to proceed with great confidence towards a career in related fields. I am eager to see where future research will take us. Special thanks is due for the patient counsel I have received from Dr. John Schwartz as a member of my master's committee. He has provided valuable perspective for this thesis work through his participation in my proposal and follow-up meetings.

This thesis would not have been possible without the support of friends and family. My parents, JJ and Mary McNelis, and my brother, Kevin McNelis, have been consistent sources of encouragement. I also appreciate all of the support from fellow graduate students: Becky Potter, Nancy Li, Larry Lu, and Adam Alsamadisi with whom I've developed timeless friendships.

# ABSTRACT

This research demonstrates the use of Light Detection and Ranging (LIDAR) for detailed measurement of volume change and erosional and depositional processes within a small gully and assessing the impact of digital elevation model (DEM) resolution on these measurements. The study site is an active gully in Meeman-Shelby Forest State Park in Tennessee, USA. DEMs were derived from an airborne LIDAR survey and multiple terrestrial LIDAR scans. DEM differences were used to quantify gross volumes of erosion and deposition within the gully over a three year period and a 49 day period. Analysis of the airborne LIDAR point cloud indicated that approximately 10,000 $m^3$ of material eroded from the bluff since the gully was formed between 1969 and 1973. A total volume of 615.8 $m^3$ of material was discharged from the gully between January 2012 (the airborne LIDAR survey) and December 2014 (the first terrestrial LIDAR survey). The surveys using the terrestrial laser scanner generated two 2 cm DEMs representing the gully terrain change during a short period of 49 days between December 2014 and February 2015. The comparison of these two DEMs indicates an estimated 2.1 $m^3$ of material was imported into the gully bottom with 11.5 $m^3$ of gross erosion and 13.6 $m^3$ of gross deposition. The same analysis performed at reduced data resolutions helped identify a turning point in the trends of erosion and deposition estimates at 0.18 m and 0.24 m resolutions, respectively, indicating that higher data densities of the LIDAR point data did not substantially improve the results. The two turning points represent the critical resolutions at which the accuracy of erosion and deposition measurements begin to deteriorate. This study demonstrates that high accuracy and density of point cloud data collected using LIDAR are capable to detect and quantify short term changes in dynamic gully systems. This study also suggests an optimum point density between 10 and 30 points per square meter to maximize efficiency of data

collection and processing. The analyses described in this thesis serve as a starting point for further monitoring development of the pool gully at very fine scales.

# TABLE OF CONTENTS

1. Introduction ..... 1
2. Literature Review ..... 4
    2.1 Gully morphology ..... 4
    2.2 Remote sensing of topography ..... 7
3. Study site ..... 15
4. Methods ..... 20
    4.1 Airborne LIDAR data overview ..... 20
    4.2 TLS data acquisition, processing, and model generation ..... 20
    4.3 Gully morphometrics ..... 29
    4.4 Scale analysis ..... 31
5. Results ..... 34
    5.1 Gully morphometrics ..... 34
    5.2 Scale analysis ..... 37
6. Discussion ..... 44
    6.1 Gully morphometrics ..... 44
        6.1.1 ALS-derived gully morphology accuracy and uncertainty ..... 44
        6.1.2 TLS-derived gully morphology ..... 47
    6.2 Scale analysis ..... 51
7. Conclusions ..... 55
References ..... 58
Appendix ..... 69
    I.Tables ..... 71
    II.Large photographs ..... 76
    III.R Segmented Regression Workflow ..... 77
    IV.R test of ASCII XYZ to array ..... 80
Vita ..... 81

# LIST OF TABLES

Table 1. List of LIDAR data sets used in the analysis .....20
Table 2. Faro Focus 3D X330 laser scanner instrument specifications .....21
Table 3. Terrestrial LIDAR survey statistics for each scan within the pool gully .....22
Table 4. Summary of volume change calculations using airborne data as baseline .....36
Table 5. Summary of volume change calculations at downsampled resolutions .....38

APPENDIX
Table A1. Resampled DEM statistics for terrestrial LIDAR survey on 12/24/2014.....71
Table A2. Resampled DEM statistics for terrestrial LIDAR survey on 02/08/2015.....72
Table A3. Residual MSE by break point from segmented regression ..... 73

# LIST OF FIGURES

Figure 1. Step angle and point spacing relationship diagram .....13
Figure 2. Diagram of beam divergence impact on surface model detail .....14
Figure 3. Study area .....16
Figure 4. Historical averages for temperature and precipitation.....15
Figure 5. Photograph of pool gully and drainage pipe.....18
Figure 6. Historical aerial photography and photographs of fallen drainage pipe ..... 19
Figure 7. Workflow for terrestrial LIDAR data acquisition and processing ..... 21
Figure 8. Terrestrial LIDAR survey (12/24/2014) scan positions ..... 23
Figure 9. Workflow for georeferencing and registration of point cloud data .....25
Figure 10. Terrestrial LIDAR scan positions outside of pool valley (02/08/2015) .....26
Figure 11. Quick Terrain Modeler grid generation settings .....27
Figure 12. Areas of interest within the pool gully .....31
Figure 13. Comparison of pre-disturbance slope and gullied slope .....34
Figure 14. ΔDEM for gully channel produced from multitemporal terrestrial LIDAR ... 36
Figure 15. Trends of minimum and maximum elevation within resampled DEMs .....36
Figure 16. Trends of erosion and deposition volumes calculated from resampled DEMs 39
Figure 17. Mean square error for segmented regression lines fit to erosion and deposition measurements by resolution.....40
Figure 18. Segmented regression fits to strongest break points..... 43
Figure 19. Lower pool gully points colorized by elevation, slope, and difference ..... 48
Figure 20. Cross sections at 4 meter intervals of lower pool gully channel ..... 49
Figure A1. Headwall material deposited in the gully channel .....75
Figure A2 The photographs were taken near the base of the gully headwall .....76

# CHAPTER ONE

## Introduction

Rapid development in the accessibility, coverage, and resolution of topographic data is improving the quality of research across a range of earth science disciplines, especially in quantifying earth surface processes. Topographic data is typically stored as a digital elevation model (DEM), representing the distribution of elevations in a raster. Two widely used DEM datasets are the Shuttle Radar Topography Mission (SRTM) (U.S. Geological Survey, 2006) DEM and the 3D Elevation Program (3DEP), formerly the National Elevation Dataset (NED) (http://nationalmap.gov/3DEP/index.html). The SRTM now offers nearly global-coverage (60° S to 60° N) DEMs of 30 m resolutions. The 3DEP DEMs are available as 1 and 1/3 arc-second, approximately 30 m and 10 m resolution, respectively, for the contiguous United States. Both SRTM and NED DEMs are invaluable resources for studying landscape processes related to climate, hydrology, ecology, and other disciplines (Farr et al., 2007; Gesch et al., 2014). However, these DEMs are not suitable for fine scale analyses (Heritage et al., 2009). Improvements in surveying technology continue to address the need for high resolution elevation data and provide updated resources for higher resolution terrain analysis.

LIDAR (Light Detection and Ranging) is a comparatively new technique to generate high resolution elevation data. Airborne laser scanning (ALS) data is typically collected and curated by commercial surveyors with refined data acquisition and processing procedures. Commercial ALS has become an established industry with growing private and public investment (Hohenthal et al., 2011) and a history of scientific applications (Notebaert et al., 2008). For example, Lohani et al. (2001) demonstrated a technique for extracting tidal basin features and deriving

geomorphological parameters, such as slope, curvature, and drainage density, from ALS data sets. Landslide inventory and characterization using ALS data was shown to be more efficient than conventional techniques when applied to a large landslide complex in Christchurch, New Zealand (McKean and Roering, 2004). ALS has also been applied in archaeological research to map shallow earthworks in lowland river valleys in England (Challis, 2006).

Terrestrial laser scanning (TLS) is common in construction and manufacturing industries, and is increasingly used in earth science research (Baltsavias, 1999; Heritage and Hetherington, 2007). However, the field and post-processing procedures specific to the use of TLS in earth science applications are still not well-defined (Heritage and Hetherington, 2007). Surveying companies utilize proprietary techniques that are not always suitable for earth science applications. Poor planning and execution of a terrestrial LIDAR survey can yield unusable data (Heritage and Hetherington, 2007). For example, improper documentation of control points and other parameters may result in datasets that cannot be fully co-registered and/or georeferenced. Because the field and processing methods of terrestrial LIDAR data are highly variable for different applications (Baltsavias, 1999), one aim of this thesis work is to establish a reliable procedure to study morphological change within a small gully using the TLS.

Despite the significant impacts of gully erosion on the landscape in recent history, few studies have focused on gullying in the Mississippi Loess soils of southwest Tennessee (Barnhardt, 1988). In this area, population boom in the early 1900s initiated a period of rapid deforestation to bolster a burgeoning hardwood industry. The transition from forest to farmland was detrimental to landscape stability and exacerbated by unregulated farming practices (Barnhardt, 1988; Barnhardt, 1989). At the peak of this agricultural activity, over 50% of the land within the park was actively farmed (Bennett, 1928). Federal officials purchased 54 $km^2$ of

land in Millington, Tennessee in 1935 to establish a public recreation area that later became the Meeman-Shelby Forest State Park (MSFSP; 35.3436°N, 90.0604°W). Remediation efforts were implemented with the goal of controlling topsoil erosion and gullying as well as preventing initiation of new gullies.

This study aims to investigate the following objectives:

- Estimate the total volume displaced from the gully since its initial development between 1969 and 1973.
- Derive high-resolution DEMs representing the gully and surrounding terrain to estimate volumetric and topographic changes.
- Examine morphological changes within the gully between January 2012 (ALS) and December 2014 (TLS1) and between December 2014 and February 2015 (TLS2) by quantifying volumes of erosion and deposition from DEMs.
- Examine the relationship between the resolution of LIDAR-derived DEMs and resulting volume measurements by performing the volumetric analysis of TLS1 and TLS2 at successively coarser resolutions.

This study will help test the following hypotheses:

1) Topographic change in the pool gully during the 49 day period can be detected and quantified using TLS.
2) An optimal point data resolution exists for monitoring the pool gully using TLS.

# CHAPTER TWO

# Literature Review

## 2.1 Gully morphology

Gullies are steep-sided linear channels that develop on hillslopes and expand through repeated flash flooding (Morgan, 1979; Bocco, 1991). Unlike ravines, the definition of a gully does not depend on the persistent presence of water. Gullies are usually referred as to have a minimum width of 0.3 meters and range from 0.5 to 30 meters in depth (Hudson, 1981). Some gullies begin as rills, smaller channels carved by surface runoff that may be formed during a single rainfall event and subsequently filled during another (Bull and Kirkby, 1997; Knighton, 1998). Steep sides and low width/depth ratios differentiate gullies from the smooth, parabolic cross-sectional profiles of stable channels (Knighton, 1998).

Surface flow is the most common driver of gully formation, but they are also initiated by landslides and piping (Morgan, 1996). Gully development in depressions left behind by landslides is common in wet climates where incising and undercutting begins rapidly with subsequent storms (Vittorini, 1972). Gullies initiated by piping, or tunnel erosion, is frequent in areas with loamy surface layers and high clay content at lower depths. Removal of vegetation by grazing or other activities causes hardening of the upper surface layer and diminished moisture retention resulting in accumulation between the two hardened upper layer and low-permeability, high clay-content lower layer (Downes, 1946). Eventual breaching of subsurface flows induces collapse of the upper soil layer, creating an initial gully depression (Zhu, 2003).

Gully development is not restricted to existing channels as they may be formed in areas without a drainage history (Ireland et al., 1939). Initial incising begins when the ability of a

landscape to resist erosion is compromised by prolonged runoff. Intermittent periods of rapid expansion and stabilization are common characteristics of both naturally-formed and human-induced gullies (Imeson and Kwaad, 1980). Observation of these periods has led to varied gully types and development stages (Bocco, 1991).

Gullies are often classified as ephemeral or permanent (Bull and Kirkby, 1997; Poesen et al., 2002). Ephemeral gullies are routinely infilled, leaving behind depressions that will ultimately promote the development of new gullies (Bull and Kirkby, 1997). Permanent gullies experience more pronounced erosion than deposition, leading to gradual enlargement, and are easily identifiable even in the absence of flowing water (Bull and Kirkby, 1997). In general, permanent gullies are formed on abandoned fields or rangelands and ephemeral gullies on excessively cultivated land (Poesen et al., 2002).

Two further gully classes were proposed by Leopold and Miller (1956): continuous and discontinuous gullies. Discontinuous gullies contain stretches of bedding with gentler slopes than the rest of the gully channel, causing a series of small fans to develop and allowing gullies to be subdivided into reaches. Continuous gullies have a more uniformed slope (Bocco, 1991; Leopold and Miller, 1956). Ireland et al. (1939) observed gullies exhibiting characteristics of discontinuous gullies at their southern Piedmont region study sites. They noted a pattern by which an initial channel cut is followed by downward incision into a weaker soil horizons and development of steep head and side walls that migrate headward through undercutting (Ireland et al., 1939; Bocco, 1991). The gullies subsequently undergo a stage of readjustment as weathering and mass wasting deposits at the base of the head and side walls, resulting in more smooth, gradual slopes. A level of equilibrium is achieved during the final stage as vegetation holds and stabilizes the terrain (Ireland et al., 1939).

Heede (1976) discussed gully behavior in the context of predicting formation and growth, hypothesizing that discontinuous gullies are simply in an earlier state of the gully formation. This claim is substantiated by the frequent presence of knick points within the channel of mature and continuous gullies that demarcate the previous extents of the various gully reaches (Ireland et al., 1939). Ultimately, gullies reach a state of equilibrium and the knick points are no longer visible (Heede, 1976).

Although the gullies can be formed naturally, gully formation has long been attributed to human influence on the landscape (Bocco, 1991). Changes in land use, such as the conversion of forest to farmland, disrupt the "natural equilibrium" of a landscape through irrigation and the diversion and concentration of surface flows (Hudson, 1981). Agricultural practices are the most common drivers of human-induced gullying, the effects of which are observed everywhere from the rainforest-turned-farmland areas of Brazil and Malaysia to the desert of the southwest United States (Morgan, 1996). The fertile topsoil layer is often the most easily eroded, a problem exacerbated by repeated tilling. Evidence suggests that threshold values for critical slope and drainage area that lead to development of gullies are higher for uncultivated land than for cropland, although these thresholds also depend on vegetation type, soil structure, and type of tilling (Poesen et al., 2003).

## 2.2 Remote sensing of topography

Studies in early publications on gully monitoring primarily utilized field measurements with erosion pins to determine change (Ireland et al., 1939; Leopold and Miller, 1956; Betts et al., 2003). The advent of modern remote sensing techniques, such as aerial photography and photogrammetry, has facilitated the study of gully dynamics using DEMs. Betts et al. (2003) used DEMs derived from photogrammetry to study erosion within New Zealand gullies over periods of 14 and 32 years. Along with the fewer hours spent in the field, this technique yielded DEMs ranging from 0.2 m to 1.65 m in spatial resolution, significantly improved the precision of the erosion estimate. They also found that the erosion rates measured from the DEMs were directly proportional to $\sqrt{A_g}$, where $A_g$ is gully area (Betts et al., 2003).

Remote sensing advances have benefitted topographical research through consistent increases in sensor resolution. LIDAR is a remote sensing technique in which a laser scanner rapidly emits pulses of energy that are intercepted by a surface and returned to the scanner. Like Radio Detection and Ranging (RADAR) and other active ranging systems, LIDAR transmits and receives electromagnetic energy, recording the amount of energy backscattered from the intercepting surface. The only difference between LIDAR and RADAR is that LIDAR systems emit shortwave energy in the near-infrared and visible range, while RADAR emits long-wavelength microwaves.

An electromagnetic wave propagates as it travels through or along a medium. The propagation of this wave of energy between transmittance and reception by the sensor is represented by the *radar equation*:

$$R = \sqrt[4]{\frac{P_s \times G^2 \times \lambda^2 \times \sigma}{P_e \times (4\pi)^3}}$$

where:

- $P_s$ is the transmitted power
- $G$ is the antenna gain
- $\lambda$ is the wavelength
- $\sigma$ is the radar cross-section
- and, $P_e$ is power returning to the sensor (W)

The radar equation can also be used to describe how LIDAR systems determine range estimates. The equation gives the power $P_E$ returning to the sensor, depending on the transmitted power $P_s$, the slant range $R$, and the radar cross-section $\sigma$ (Wolff, 2016). The reflected power $P_r$ at the intercepting surface is required to determine the power $P_E$ returning to the sensor. Reflected power $P_r$ depends on the power density $S_u$, antenna gain $G$, and radar cross section $\sigma$ (Wolff, 2016). The radar cross section $\sigma$ is the reflective ability of the target surface and is dependent on its shape and material composition, and the direction and frequency of the intercepting laser. Antenna gain $G$ is the effect of redistributing radiated power to provide a stronger signal in one direction (Wolff, 2016). The power density $S_u$ of a transmitter in all directions is given in watts/m$^2$ by (Wolff, 2016):

$$S_u = \frac{P_s}{4 \times \pi \times R^2}$$

where:

- $P_s$ is the transmitted power
- $S_u$ is the nondirectional power density
- And, $R$ is the range from the antenna to the target surface

The directional power density is equal to the nondirectional power density multiplied by the antenna gain. The power returning to the sensor $P_e$ in watts (W) is found by (Wolff, 2016):

$$P_e = \frac{P_s \times G^2 \times \sigma \times \lambda^2}{(4\times\pi)^3 \times R^4}$$

where:

- $P_s$ is the transmitted power
- $\sigma$ is the cross-section
- $\lambda$ is the wavelength
- and, $R$ is the range

The radar equation takes into account all factors influencing the wave propagation of an emitted pulse (Wolff, 2016).

LIDAR survey has become the preeminent technique for gathering the high resolution elevation data used to generate DEMs (Cavalli et al., 2008; Hohenthal et al., 2011; Marks and Bates, 2000). Point data collected using LIDAR systems are referred to as point clouds (Heritage and Hetherington, 2007). Each point in the cloud includes 3-dimensional coordinates (x, y, z) that are often accompanied by an intensity value that represents the ratio of the strength of the reflected pulse returned from the intercepted surface to the strength of the pulse at its emittance (Cang et al., 2013; Kaasalainen et al., 2011; Kukko et al., 2008). Intensity values are dependent upon a number of factors, including but not limited to, wavelength, range, reflectivity of the surface, presence of ambient light, humidity, and the laser's perpendicularity to the surface, also known as the incidence angle (Cang et al., 2013).

The position accuracy in spatial data is commonly measured by Root Mean Square Error (RMSE) between control points within the spatial data set and ground truth measurements. The RMSE can also be calculated to describe the registration error between two LIDAR point clouds.

The National Standard for Spatial Data Accuracy (NSSDA) determines the RMSE as the square root of the average of a sample of squared differences between the data set being measured and a reference data set (Federal Geographic Data Committee, 1998). Equation 2 shows the RMSE calculations using a set of points to quantify the registration accuracy of a transformed point cloud to a reference point cloud (Federal Geographic Data Committee, 1998; Toth, 2014):

$$RMSE_r = \sqrt{\frac{\Sigma((x_{data,i}-x_{reference,i})^2+(y_{data,i}-y_{reference,i})^2)}{n}} \qquad (2)$$

where:

- $x_{data,i}$ and $y_{data,i}$ are coordinates of point *i* within the point cloud being tested for registration accuracy
- $x_{reference,i}$ and $y_{reference,i}$ are coordinates of the corresponding point *i* within the reference point cloud
- *n* is the number of sampled points used to compute RMSE
- *i* is an integer from 1 to *n*

Two primary methods for gathering LIDAR data are airborne (ALS) and terrestrial laser scanning (TLS) (Heritage and Hetherington, 2007). Although similar in function, applications vary significantly between them (Baltsavias, 1999; Heritage and Hetherington, 2007). An ALS is better suited for data acquisition that necessitates coverage over areas of 1 $km^2$ or larger, while a TLS is often conducted for smaller areas. ALS and TLS also differ greatly in the resolution of the resultant data. The spatial resolution of data collected by ALS is typically between 1 m and 3 m, while a TLS can yield data at the centimeter scale (Hohenthal et al., 2011).

Types of LIDAR can be further divided into discrete return and waveform. The waveform LIDAR systems record the full return of an emitted pulse, so that an emitted pulse may return multiple backscattered pulses to the sensor. Discrete return systems only record one return per emitted pulse (Wagner et al., 2006; Hohenthal et al., 2011). In waveform systems, the

return number of collected points is stored as an additional attribute that is often used to separate bare earth from the remainder of the point cloud (Heritage and Hetherington, 2007).

Like other remote sensing techniques, LIDAR is subject to a trade-off between spatial resolution and coverage (Heritage et al., 2009; Hodge et al., 2009; Milan et al., 2007; Rumsby et al., 2008). For example, TLS has proven effective in quantifying morphological change following minor flooding events at the reach scale (Picco et al., 2013), while ALS is more suitable for the study of major events at the basin scale (Croke et al., 2013). Perroy et al. (2010) used a combination of airborne and terrestrial LIDAR to measure annual volumetric soil loss due to gully erosion in a watershed on Santa Cruz Island, California. Their results were validated by comparing measurements taken using LIDAR to existing geomorphic and geodetic survey data gathered using total stations (Perroy et al., 2010). ALS and TLS methods have also been evaluated in terms of their suitability to monitor seacliff changes over a 6 month period along a 400 m coastline in Del Mar, California (Young et al., 2010). Variations in cliff face volume changes measured using both methods were strongly correlated. But the TLS data captured small changes more consistently and a greater volume of change overall. The researchers noted that the ALS data can be gathered very rapidly; in comparison, TLS can provide better coverage of areas at the base of the sea cliff (Young et al., 2010).

Both ALS and TLS have been used extensively for the study of erosion and deposition at a variety of temporal scales, but their advantages are most pronounced when applied at short time intervals (Bangen et al., 2014; Corsini et al., 2013; Croke et al., 2013; Kukko et al., 2008). The high spatial resolution of the data produced using LIDAR captures minor changes in microtopography occurring over a period of months or years that would be immeasurable using traditional remote sensing methods (Hohenthal et al., 2011).

A TLS operator must consider critical parameters, such as point spacing, range, and field of view (FOV), when preparing a survey (Carr et al., 2013). These parameters are set to ensure that point density, the number of points per unit area, is enough to produce surface models at a desired resolution. The FOV is an angular measure of the extent of the viewshed of the TLS. The scanner should be set to a vertical and horizontal FOV large enough to fully capture the surface of interest (Zhu et al., 2008; Carr et al., 2013). The point spacing should be set to ensure that the average distance between points is less than or equal to the desired model resolution at the specified range (Zhu et al., 2008). Optimizing scan parameters requires additional consideration of instrument-specific parameters, such as step angle, laser beam strength, diameter, and divergence (Carr et al., 2013). The step angle of a scanner determines the degree of rotation between the emittance of each successive laser pulse. Point spacing at a given range is a function of step angle where point spacing equals to the distance times the tangent of the step angle (Carr et al., 2013). The relationship of step angle and point spacing is illustrated in Figure 1.

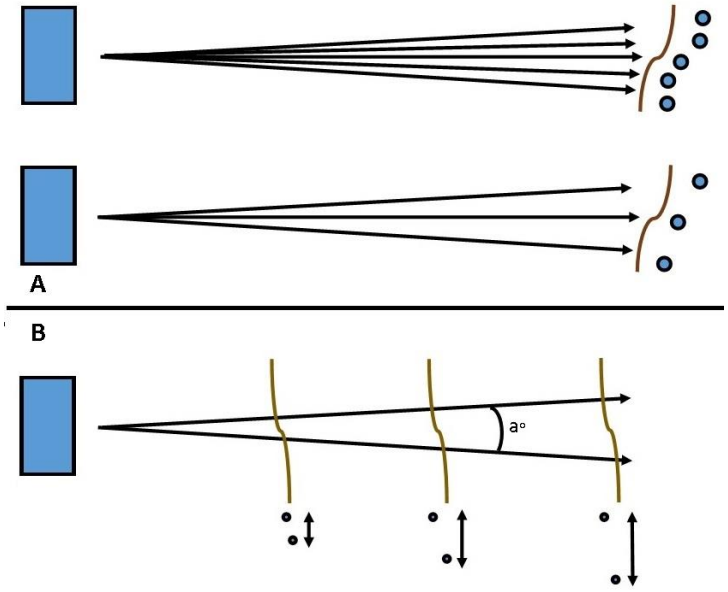



Figure 1. A) A larger step angle results in greater point spacing. The example diagram in A shows that the number of points captured for an equal surface area are reduced from five to three by increasing the size of the step angle between emitted pulses from the scanner (Carr et al., 2013); B) Point spacing increases as distance from the scanner increases (Carr et al., 2013).

Laser beam diameter and divergence of the TLS instrument should also be considered when preparing a survey because of their impact on resultant point density. The diameter of the laser at the point of contact with a surface, the laser "foot print", increases with increasing distance of the intercepting surface from the scanner (Zhu et al., 2008). This rate of increase is an angular measure referred to as the beam divergence and is dependent upon the laser strength, or the wavelength at which the light is emitted, and its initial diameter (Zhu et al., 2008). Divergence is given by (Carr et al., 2013):

$$\theta = 2 \times \arctan\left(\frac{D_f - D_i}{2 \times l}\right)$$

where:

- Θ is beam divergence
- $D_f$ and $D_i$ is the beam diameter at two separate points, and

- $l$ is the distance between $D_f$ and $D_i$

Figure 2 depicts the diminished surface detail captured by three differently sized laser footprints. Point cloud detail is diminished at excessive distances from the scanner due to this increase in laser foot print diameter.

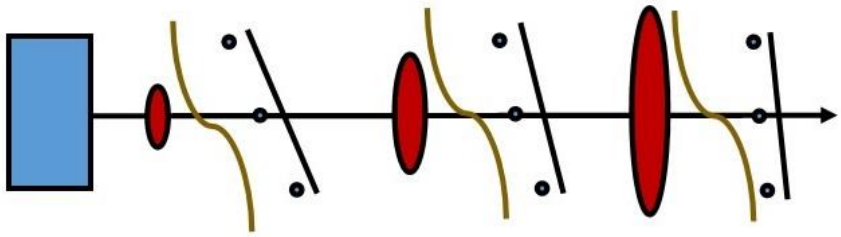


Figure 2. Depiction of how beam divergence can impact the detail of captured points. The three laser foot prints are intercepting the same hypothetical surface at unknown ranges. The smallest foot print returns the best range estimate because it illuminates the surface around the laser nadir with the highest precision (Carr et al., 2013).

# CHAPTER THREE

## Study Site

The study site for this research is a gully within the Meeman-Shelby Forest State Park (MSFSP) located north of Memphis in Shelby County, Tennessee (Figure 3). The park is along the eastern bluff of the Mississippi River and covers 54.5 $km^2$. It is one of the most visited state parks in Tennessee (Tennessee State Parks 2016). MSFSP and its surrounding areas are prone to gully formation due to human and environmental factors, such as land use history and silt loam soils. Shelby County has a humid subtropical (*Cfa*) climate according to the Köppen climate classification. Temperatures peak in July with average highs and lows of 33° C (92° F) and 23° C (74° F), respectively. January is the coldest month with average highs and lows of 9.9° C (50° F) and 0.3° C (33° F), respectively. Shelby County averages 1.36 m (4.47 ft) of precipitation per year with much occurring in the early winter and spring months (U.S. Climate Data 2016). Historical monthly averages for high and low temperature and precipitation for Shelby County are illustrated in Figure 4.

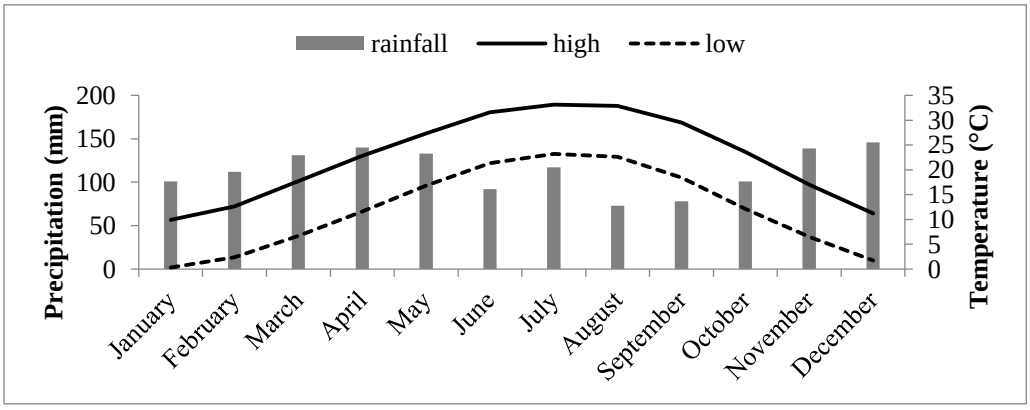



Figure 4. Historical (1981-2010) monthly average high and low temperature and precipitation for Shelby County, Tennessee (U.S. Climate Data 2016).

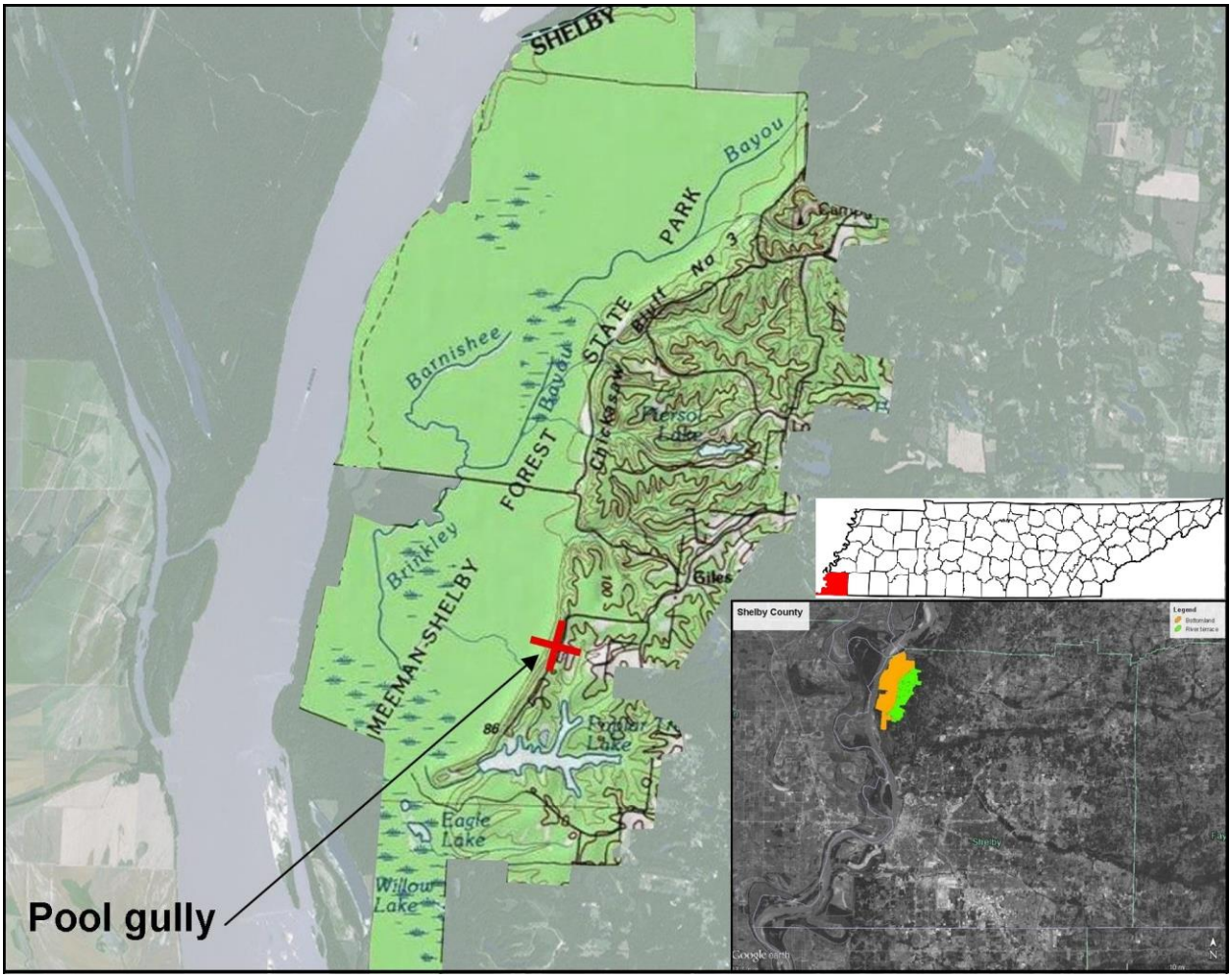



Figure 3. Location of the pool gully site is marked with a red 'X' on the topographic map of Meeman-Shelby Forest State Park. The inset map shows all of Shelby County, Tennessee – orange and green filled areas are the bottomland and river terrace sections of the park, respectively.

Mississippi river floodplain comprises the western half of the land area in MSFSP. Hardwood forest featuring bald cypress (*Taxodium distichum*) and Tupelo swamp (*Nyssa biflora*) covers the bottomland that floods episodically during spring months (Tennessee State Parks 2016). The Mississippi river terrace, known locally as the Chickasaw Bluff, bisects the park, rising abruptly from the bottomland to higher elevations in the eastern half of the park (Barnhardt, 1988; Tennessee State Parks 2016). Species of oak (*Quercus*), beech (*Fagus*), hickory (*Carya*), and sweet gum (*Liquidambar*) trees cover the river terrace and provide a habitat for hundreds of bird species as well as deer and small mammals, such as beaver and fox (Barnhardt, 1988; Tennessee State Parks 2016).

Barnhardt (1989) examined the effectiveness of the extensive soil conservation program in the MSFSP. The federal government acquired the land in 1935 to establish a "recreational demonstration area" managed by the National Park Service. The project included major reclamation efforts. Hundreds of check dams were constructed within active gully channels and, in some cases, the channels were re-engineered entirely. Barnhardt (1989) concluded that mitigation efforts were largely ineffective, as heavy rainfall events tend to re-invigorate gully activity, although certain areas appeared to have achieved a degree of stability.

This study focuses on a "pool gully" (Figure 5) formed at the out spout of the drainage system for a nearby pool. The gully is carving into the river terrace of the Mississippi River and was formed after the drainage system was engineered. The gully is approximately 30 m at its widest, with a headwall depth of approximately 20 m and a length of 90 m. The catchment area of the pool deck is approximately 4070 $m^2$. The 18 inch pipe discharges drainage from the pool deck as well as a biweekly flush of significant volumes of water for filter maintenance during operational months of May, June, and July, also known as backwashing. The pool has a

perimeter of 150 m and a water capacity of approximately 75,000 gallons. Public pools typically have a turnover of 6 to 8 hours, meaning that the full capacity of the water circulates through the pump over that period (Pool and Spa, 2016). A 75,000 gallon pool with a 6-hour or 8-hour turnover will have approximate flow rates of 208 and 156 gallons per minute (gpm), respectively (Pool and Spa, 2016). A pool of comparable size and flow rate is expected to backwash at a rate of approximately 280 gpm due to back pressure. The recommended backwash frequency and duration depends on the number of patrons (Pool and Spa, 2016). Assuming a backwash duration of 30 minutes, at 280 gpm the biweekly discharge due to backwashing is approximately 8400 gallons of water.



Figure 5. Photograph of the pool gully channel. The drainage pipe is visible inside the red box at the top of the photograph.

In our conversation, park authorities estimated that the pool was constructed at some point during the 1960s. They also acknowledged the pool valley's impressive size and rapid growth. We examined available historical aerial photography in this area to investigate the time when the pool was built. The left aerial photograph in Figure 6 reveals that the pool is absent on February 13, 1969. The pool is visible in the right photograph, indicating it was constructed before April 12, 1973. Assuming that initial incision into the bluff was a consequence of pool drainage, we estimate that the pool valley formed between 1969 and 1973.

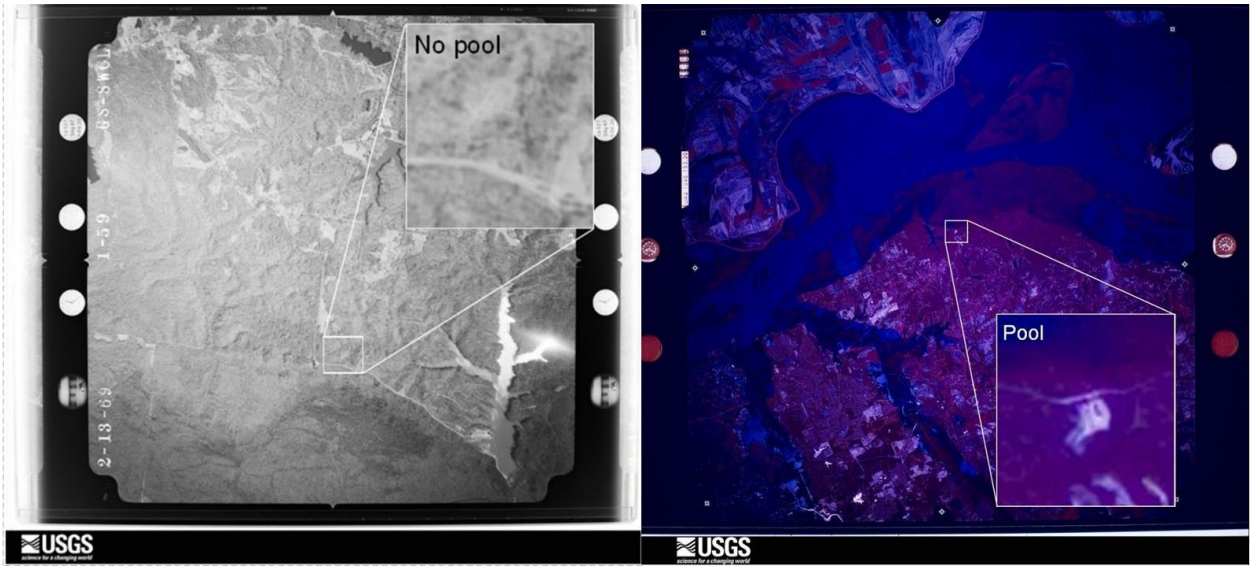



Figure 6. The two aerial photos indicate that the pool at Meeman-Shelby Forest State Park was constructed between 02/13/1969 and 04/12/1973. Left: AR1SWCL00010059, 02/13/1969, 1:20500; Right: AR5730010929044, 04/12/1973, 1:131000
Source: United States Geological Survey

# CHAPTER FOUR

# Methods

## 4.1 Airborne LIDAR data overview

An airborne LIDAR survey of Shelby County, Tennessee, was conducted by the United States Geological Survey (USGS) in January 2012. The data was gathered at a maximum nominal point spacing of < 1 m with the goal to improve the accuracy and precision of the 1/9 arc-second (3-meter) National Elevation Dataset (NED). A Leica ALS50-II 150 kHz LIDAR instrument was flown on a Cessna 404 aircraft. Instrument specifications for the Leica system are detailed in Table 1 of Appendix III. Additional details of the airborne LIDAR survey are also described in Appendix III (Woolpert, 2012).

Table 1. LIDAR data sets used in the analysis

| Sensor | Date | Type | Coverage | Spatial Reference | Source |
|---|---|---|---|---|---|
| ALS * | 1/24/2012 | Cloud | Shelby County | NAD83 UTM 16N | Leica ALS50-II |
| TLS (5) ** | 12/24/2014 | Cloud | Gully | NAD83 UTM 16N | Faro Focus 3D X330 |
| TLS (10) ** | 2/8/2015 | Cloud | Gully & parking | NAD83 UTM 16N | Faro Focus 3D X330 |

* Airborne laser scanning product of LIDAR campaign commissioned by the United States Geological Survey, January 2012

** Terrestrial laser scanning data sets and the total number of scans in parenthesis

## 4.2 TLS data acquisition, processing, and model generation

Gathering the TLS data and preparing it for analysis required much planning and effort. The workflow for data acquisition is illustrated in Figure 7. Heritage and Hetherington (2007) noted that parameterization of a TLS survey is dependent on the application as well as the make

and model of the LIDAR instrument. The TLS used for both surveys was a FARO Focus 3D X 330 laser scanner. The instrument specifications are listed in Table 2.

Table 2. Faro Focus 3D X330 terrestrial laser scanner technical specifications

| Parameter | Faro Focus 3D Specifications |
|---|---|
| Range | 0.6 m to 330 m to a 90% reflective surface |
| Measurement Speed | 122000 to 976000 points/second |
| Ranging Error | +- 2 mm |
| Vert. / Horiz. FOV | 300 / 360 degrees |
| Step Angle | 0.009 degrees |
| Laser Class | Class I laser product (FDA CFR 21) |
| Wavelength | 1550 nm |
| Beam Divergence | 0.19 mrad @ $1/e^2$ |
| Beam Diameter at Exit | 2.25 mm @ $1/e^2$ |
| Additional Sensors | Dual axis compensator (levels each scan, accurate to 0.015 degrees), barometer, compass, GNSS |

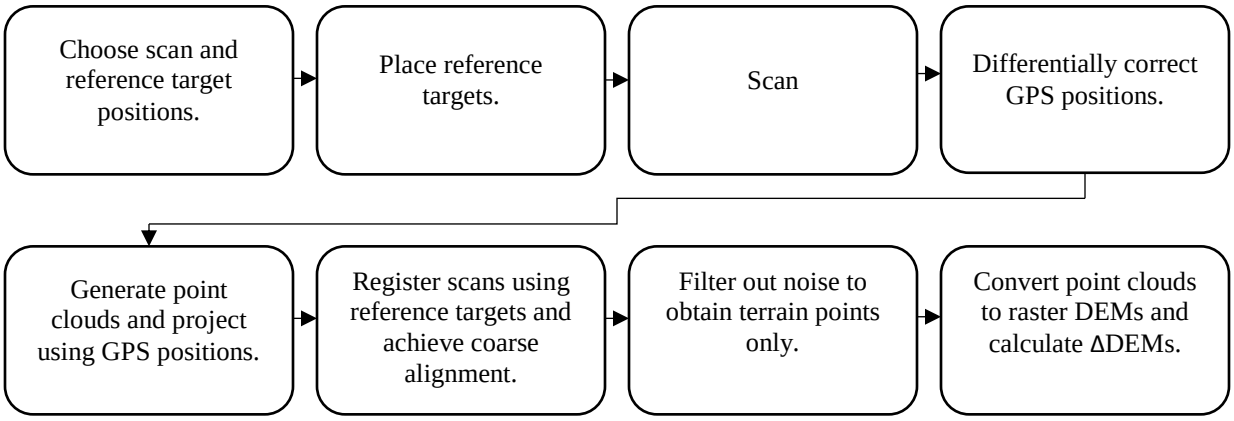



Figure 7. General workflow for data acquisition and processing with the terrestrial laser scanner

TLS data were collected on 12/24/2014 and 2/8/2015 to generate DEMs of sufficient resolution to detect micro-topographical change within the gully channel. A fundamental element of planning was to choose and document well-distributed positions of both the scanner

instrument and stationary scan registration around the gully. The registration points were later used to place the scans into the proper orientation relative to each other. A total of five scans per survey were collected within the gully for each of the two TLS surveys. General information about the scans within the pool valley is listed in Table 3. An additional five scans were also performed outside the gully during TLS2. Taking into consideration best practices outlined by Carr et al. (2013), the TLS positions were chosen based on the following considerations: a) a minimum of 4 control points were within the viewshed of the scanner; b) substantial overlap existed between scanning viewsheds; c) topographic shadow, or areas shielded from view of the scanner due to relief, was minimized; d) areas of interest were scanned from multiple perspectives; and e) the TLS was placed atop the tripod above relevant terrain features and at a consistent height (1.65 m). Figure 8 illustrates the positions of the scanner for the TLS survey conducted on December 24, 2014.

Table 3. Terrestrial LIDAR survey statistics for the five scans performed within the gully on December 24, 2014 and February 8, 2015. The scanner was set to emit approximately 43,267,380 total pulses within a 360° horizontal field of view and 300° vertical field of view.

| Scan ID | Date | Latitude, Longitude | Total Points | RMSE (m) |
|---|---|---|---|---|
| TLS1001 | 12/24/2014 | 35.317433, -90.061229 | 24,508,783 | **0.014 (avg)** |
| TLS1002 | 12/24/2014 | 35.317370, -90.061180 | 26,262,629 | 0.0091 |
| TLS1003 | 12/24/2014 | 35.317439, -90.061103 | 27,640,332 | 0.0163 |
| TLS1004 | 12/24/2014 | 35.317376, -90.060990 | 29,393,729 | 0.0152 |
| TLS1005 | 12/24/2014 | 35.317267, -90.060976 | 32,786,140 | 0.0148 |
| TLS2001 | 02/08/2015 | 35.317462, -90.061219 | 25,613,229 | **0.017 (avg)** |
| TLS2002 | 02/08/2015 | 35.317382, -90.061169 | 27,428,903 | 0.0194 |
| TLS2003 | 02/08/2015 | 35.317443, -90.061052 | 27,913,785 | 0.0201 |
| TLS2004 | 02/08/2015 | 35.317413, -90.060974 | 29,323,810 | 0.0161 |
| TLS2005 | 02/08/2015 | 35.317336, -90.060948 | 31,745,204 | 0.0133 |

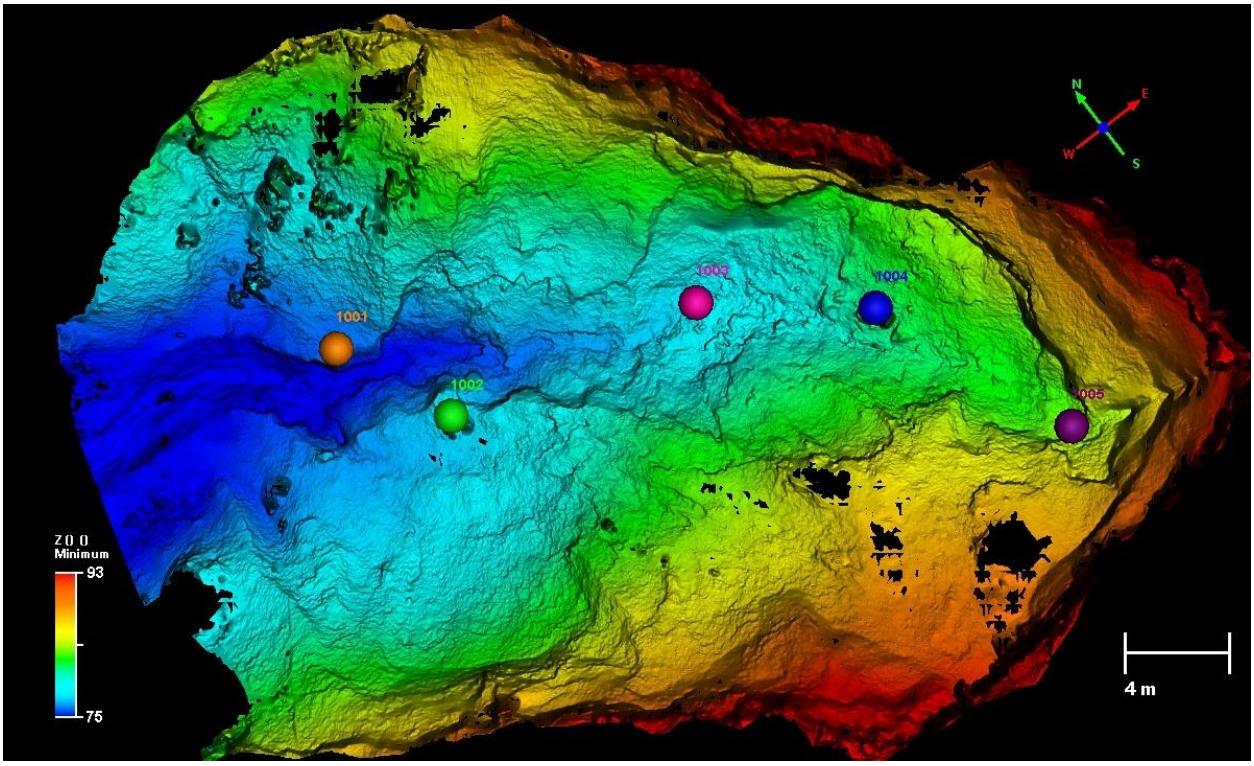



Figure 8. Scan positions for the survey of the gully performed on 12/24/2014 overlaid upon a mesh produced from the ground points from the merged point clouds. Black areas are gaps with too few points to interpolate.

The TLS was set to collect points with 0.02 m spacing at a range of 20 m for the two TLS surveys of the pool gully. These specifications should yield point cloud data with enough detail to produce DEMs at 0.02 m resolution, deemed suitable for the purpose of this study to capture short term changes in topography. Point spacing for segments of the gully channel within 20 m of the scan positions did not exceed 0.02 m. Increases in beam diameter are negligible at this range and were not considered. The scanner was set for a 360° horizontal FOV and a 300° vertical FOV, so that points were captured in all directions except the circular area over 60 degrees below the horizontal plane of the scanner. Each scan took 08:09 (MM:SS) to perform 43,267,380 measurements. Fewer points exist in the resulting clouds because emitted pulses that do not intercept a surface will not return point measurements. The TLS captured an average of

28,261,654 points per scan across all scans within the gully. For each survey, the total number of points collected increased with each sequential scan because of increasing surface area as scan positions moved deeper into the gully (Table 3).

GPS measurements were taken using a Trimble GeoXH at each scan and each target position. The GPS readings were differentially corrected to ensure optimal co-registration among the TLS point clouds. Due to the depth of the pool valley, the receiver periodically lost connection to some or all GNSS satellites. For this reason, positions were recorded for a minimum of 10 minutes at 5 second intervals. The GPS positions were differentially corrected and applied to the scan files (.fls) with Faro Scene version 5.3.3 software (Faro Technologies) to ensure proper registration. Differential correction took place in the Trimble GPS Pathfinder Office version 4.10 software (Trimble Inc.). Position records were excluded if fewer than 4 GNSS satellites were overhead and/or fewer than 5 nearby base stations were pinged at the time of recording. They were also excluded if horizontal uncertainty was greater than 15 cm after differential correction. Differentially corrected GPS positions were compiled for each reference target and scan location and a representative average position was determined for each.

Corrected GPS positions were applied to each of the scans so that we were confident that the center point of each was within 15 cm of the actual location. Reference targets were found in each of the scans and were assigned corresponding labels and GPS positions. With each additional reference, the scans were transformed to better reflect the true locations of the contained points. When each reference targets had been assigned GPS positions, the scan points are close to their true position and orientation. The locations of the individual scans were refined further using the Cloud-to-Cloud registration tool in SCENE. The most centrally-located scan was set as the reference scan and the remaining four were transformed to match. The software

provides registration accuracy as the computed RMSE for a set of points within each transformed scan to the reference scan. The distance of each reference target, referred to as “tie points” in Faro Scene, within the transformed scans to its predicted position within the reference scan is also computed as a measure of accuracy. The Scene software returns a tie point “tension” in meters representing the distance from the tie point to the predicted position of the tie point after cloud transformation. High tie point tension indicates it might be negatively influencing overall registration accuracy. Tie points with tensions greater than 0.1 m were removed and Cloud-to-Cloud registration performed again, reverting transformations when registration accuracy was diminished and excluding tie points when accuracy improved until the best the registration was achieved. The general process for georeferencing and registration of the TLS point clouds is depicted in the flow chart in Figure 9.

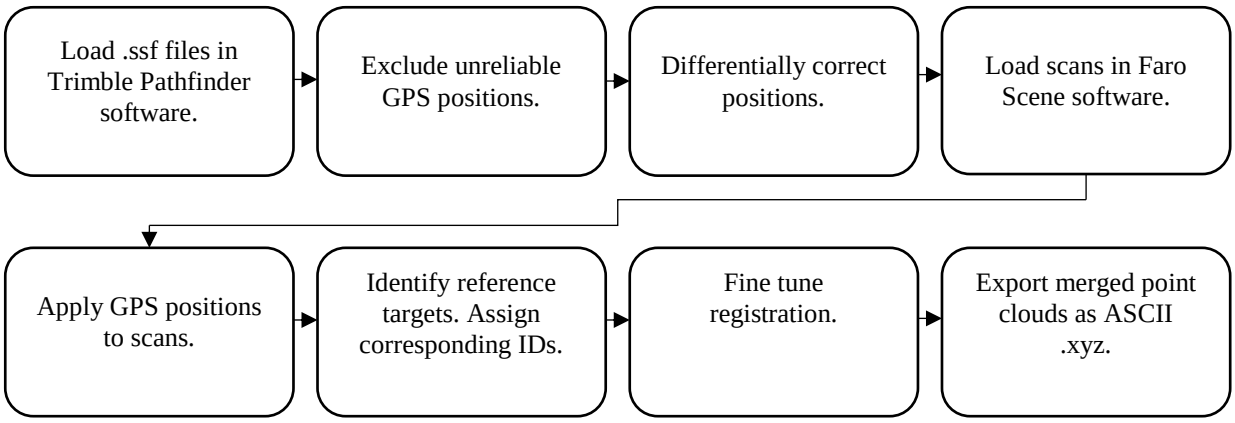



Figure 9. Flow chart describing the process for georeferencing and co-registration of the TLS point cloud data

An additional measure was taken to ensure adequate registration of the ALS and TLS point clouds because of the lack of control points and uncertainty of the TLS1 and TLS2 scan

positions determined using GPS. The positions of the five scans performed outside of the pool valley during TLS2 are depicted in Figure 10 along with terrain points from the ALS survey. Utility poles as well as the corners of the swimming pool and nearby structures were treated as control points within the ALS survey and matched to equivalent points captured by the nearby scans from TLS2 using tools within the open source Cloud Compare version 2.6 software. Registration of the TLS2 point cloud to the ALS point cloud yielded a 4x4 transformation matrix that captured the rotation and translation from its original orientation. The transformation matrix was applied to the TLS1 point cloud to reconcile its registration with the TLS2 point cloud so that all three achieved the highest possible co-registration.

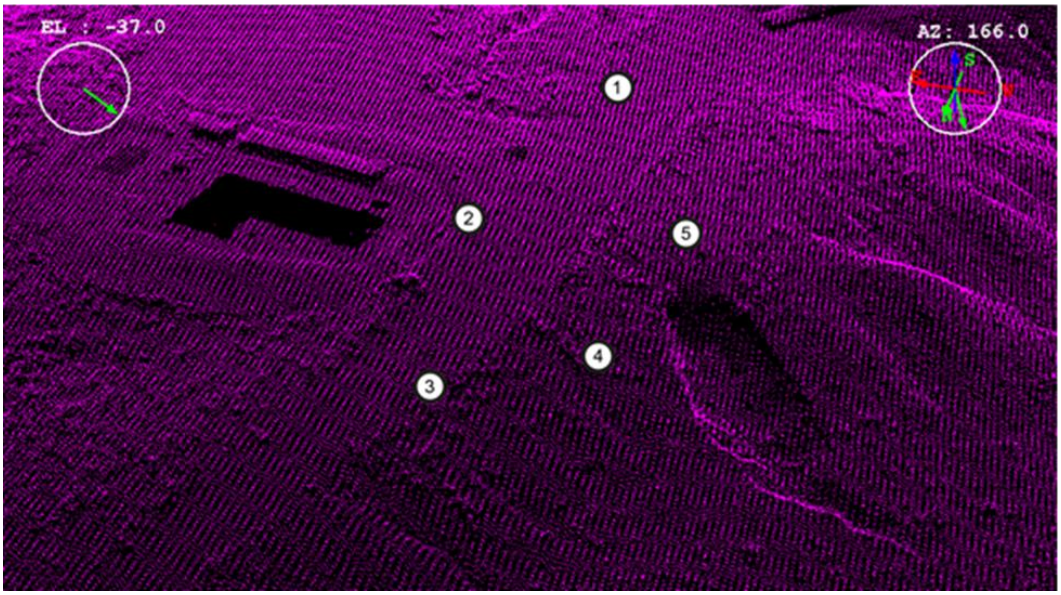



Figure 10. Scans were performed outside of the pool gully to improve registration between the airborne LIDAR point cloud and the terrestrial LIDAR point cloud from 02/08/2015.

After point cloud co-registration, points representing vegetation and other noise were removed to generate the DEMs from the points representing the bare-earth terrain. This process

was performed using a combination of tools provided within the commercial software Quick Terrain Modeler (QTM) 8.0.4 (Applied Imagery, LLC). Extracting bare-earth points from the ALS point cloud was relatively straightforward using the last returns of the point clouds. An interpolated surface was generated from the last returns in the ALS cloud using QTM. The screenshot in Figure 11 shows the grid generation options available to users through QTM. The default interpolation method is called adaptive triangulation. This method populates cells of a grid with the max, mean, or min Z of points that fall within each, where possible. If a cell contains no points but at least 5 adjacent cells are valid, simple interpolation is used to determine the cell value. Larger gaps are filled using Delaunay Triangulation.

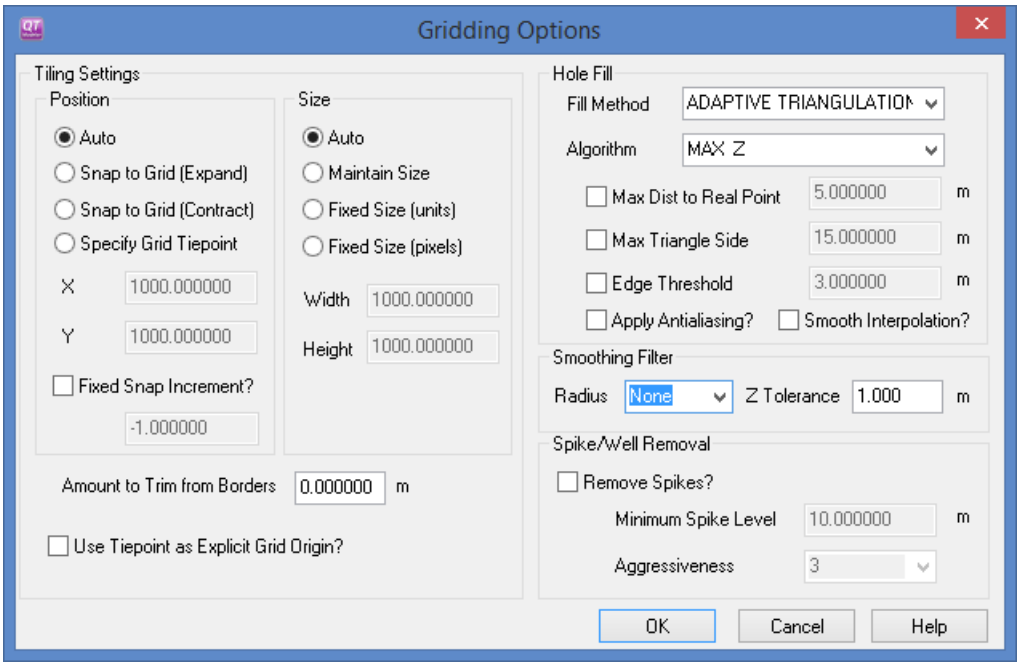



Figure 11. Settings in Quick Terrain Modeler 8.0.4 for conversion of point cloud data to gridded data.

The amount of effort required to remove noise depends on the complexity of terrain and typically involves various combinations and iterations of common grid statistics (Hofle et al., 2013). The near-vertical sidewalls in portions of the pool gully complicated noise removal because they can be misrepresented by statistics calculated within a horizontal grid. To address this issue, a preliminary step was taken by slicing the clouds into subsets at 5 meter vertical intervals. The majority of non-terrain points in each subset were identified and removed with relative ease through visual examination. After the preliminary noise removal, the slices were merged back into a single cloud for each TLS1 and TLS2.

After slicing and re-merging, most of the points represent the terrain, with the remaining noise clustered too close to the ground to be visibly distinguished. This noise was removed using the Above Ground Level (AGL) Analyst within QTM. The AGL Analyst estimates ground level by determining the minimum elevation within each cell of a horizontal grid. Points are assigned values equal to the height above the minimum elevation within each grid cell. Choosing a grid of the appropriate size is critical to using this tool effectively. A grid finer than the average density of the ground points will cause the lowest elevation in some grid cells to be measured from above-ground points. Alternatively, a grid that is too coarse will result in a loss of detail when filtering based on assigned heights above the terrain. A ground level estimate was calculated within a 0.02 m grid for both point clouds using the AGL Analyst and points were assigned AGL values. The grid size and slope of the terrain was considered when filtering noise based on the AGL values. With an estimated maximum slope of the gully sidewalls of approximately 75 degrees and a grid cell size of 0.02 m used to calculate AGL values, it was determined that points with AGL values less than or equal to 0.07 m could represent terrain points in areas with the steepest slope. For this reason, only points with AGL values greater than 0.07 m were removed.

The two point clouds were almost entirely ground points after filtering with the AGL Analyst. The final step in removing noise near the terrain was to calculate slope for the points within a fine horizontal grid. Local slope values were assigned to the points within a 0.01 m grid and points with slope values greater than 75 degrees were removed. The slope-based filter was effective in removing the remaining noise because non-ground points typically result in a slope approaching 90 degrees when compared to the points within adjacent cells. The adaptive triangulation method mentioned previously was used to generate DEMs from the remaining ground points.

## 4.3 Gully morphometrics

Terrain points within the pool gully were removed from the ALS point cloud and interpolated to create an estimated model of the "undisturbed" slope of the river terrace. The volume of material exported from the entire gully since initiation was estimated by calculating the volume between the estimated undisturbed slope and the ALS-derived gully DEM. This analysis was performed in QTM using the "Volume Calculation" tool.

A different method was used to estimate volumes of erosion and deposition over the shorter time intervals. Change detection between two DEMs is performed by deriving a DEM of difference (ΔDEM) (Croke et al., 2013; James et al. 2007; Thoma et al. 2005). A ΔDEM is a grid equal in area to the intersection of two input DEMs and contains calculated values equaling to the elevation difference between corresponding grid cells. This method has been used to effectively measure relative quantities of erosion and deposition. When the DEM from a later observation is subtracted from the DEM from an earlier observation, the sum of the positive values within a ΔDEM equals to the gross volume of material lost from cells that experienced net

erosion and the sum of the negative values equals to the gross volume of material gained by cells that experienced net deposition. The same method was applied to this study to analyze the geomorphic change within the pool gully channel. The following equations represent the ΔDEM calculations used to quantify topographic change within the gully:

1) $DEM_{ALS\ 2012} - DEM_{TLS\ 2014} = \Delta DEM$; $DEM_{ALS\ 2012} - DEM_{TLS\ 2015} = \Delta DEM$
2) $DEM_{TLS1} - DEM_{TLS2} = \Delta DEM$

The DEM from TLS1 was treated as the baseline to derive the ΔDEM for TLS2. The resulting volumes of TLS1 DEM above and below the TLS2 DEM represent the volumes of erosion and deposition that occurred between the two surveys, respectively. To better understand the differences in short term gully morphology, three areas of interest were chosen in the topographically distinct segments for detailed examination: the *gully channel*, *gully head*, and *left wall* areas (Figure 12). The *gully channel* area represents the portion of the gully that meets the maximum slope criteria for DEM generation mentioned in the previous section. The *gully head* and *left wall* areas are subsets of the *gully channel* that were chosen because much of the geomorphic change detected through the ΔDEM analysis was concentrated in these two areas. The *gully head* area is located directly beneath where the drainage pipe breaches the gully headwall. The *left wall* is a portion of the left sidewall of the gully where considerable mass wasting is evident in the ΔDEM.

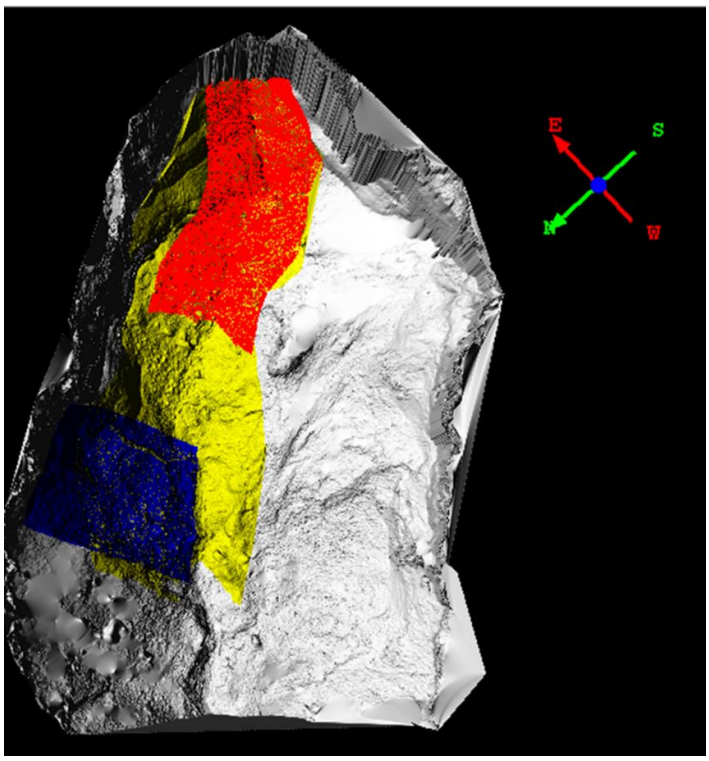



Figure 12. Areas of interest within the pool gully: *gully channel* (yellow), *gully head* (red), and *left wall* (blue).

## 4.4 Scale analysis

The sensitivity of topographic measurements to the resolution of a DEM has been investigated (Zhang and Montgomery, 1994; Yang et al., 2010). Comparisons of measurements from DEMs with resolutions equivalent to those available in popular elevation datasets such as the NED and SRTM have shown a large disparity in derived topographic attributes (Huaxing et al., 2006; Deng et al., 2007; Sorensen and Seibert, 2007). Although topographic measurements on high-resolution DEMs are more precise than on lower-resolution DEMs, the benefit of this increased resolution varies with the geographical scale of the application. High data resolution coincides with high data volume and high volume data is inherently more cumbersome than low volume data; thus, data resolution exceeding that necessary for a particular application makes

analysis less efficient. Zhang and Montgomery (1994) noted substantial differences in slope and drainage area measurements from DEMs of simulated landscapes at 2, 4, 10, 30, and 90 m resolution. Despite these differences, they concluded that 10 m DEMs are a compromise between data resolution and volume at the landscape scale. Yang et al. (2010) conducted a similar scale experiment to delineate stream networks using DEMs between 1 and 60 m resolution produced from airborne LIDAR data. They concluded that 10 m DEMs were most appropriate for extracting stream channels at the landscape scale. The scale analysis conducted in this study aims to examine similar effects of the influence of DEM resolution on terrain analysis results when applied to smaller scales through the study of microtopography within the pool gully.

To conduct the scale analysis, the two TLS point clouds were incrementally resampled in QTM from 0.02 m to match the 0.66 m resolution of the ALS model. Change volume was calculated for each resolution and plotted for visual interpretation of the relationship between resolution and measurement results. For both erosion and deposition, a distinct change in the relationship of volume measurements to resolution is apparent as resolution decreases. The volume calculations were fit with segmented regression analysis by resolution to determine the resolution at which the behavior of the erosion and depositions volumes begin to change. Segmented regression, also known as piecewise or broken-stick regression, is used when a variable $x$ is thought to predict $y$ differently over certain ranges of $x$ (Netter et al., 1990). This method is commonly used in scientific fields to measure abrupt changes in relationship at some point of significance for the independent variable, and to model thresholds. For example, segmented regression is used in medicinal studies to gauge the impact of an introduced treatment (Netter et al., 1990). Ecological studies use it to determine thresholds for factors related to species survivability, such as habitat loss (Toms and Lesperance, 2003). In geomorphology,

segmented regression has been used to identify distinct phases in rates of bedload transport (Ryan and Porth, 2007). Segmented regression analysis is applied to our data to check for the existence of a threshold in resolution where the behavior of measured volumes of erosion and deposition changes. The strength of the regressions were evaluated by $R^2$ and p-values and examined by the residual mean square error (MSE) of each and the threshold resolution was determined by the regression with the lowest MSE. The MSE measures the vertical spread of the data points around the regression line. An annotated R workflow is included in Appendix IV.

# CHAPTER FIVE

# Results

## 5.1 Gully morphometrics

The estimated total volume of material exported from the entire pool gully since its initiation was determined by calculating the volume difference between the interpolated undisturbed slope and the gullied slope DEMs generated from the ALS point cloud. The two models used to perform this analysis are illustrated in Figure 13. The volume difference between the two DEMs indicates that an estimated 9985.9 $m^3$ of material has been displaced from the original bluff slope since the pool and drainage pipe were installed.

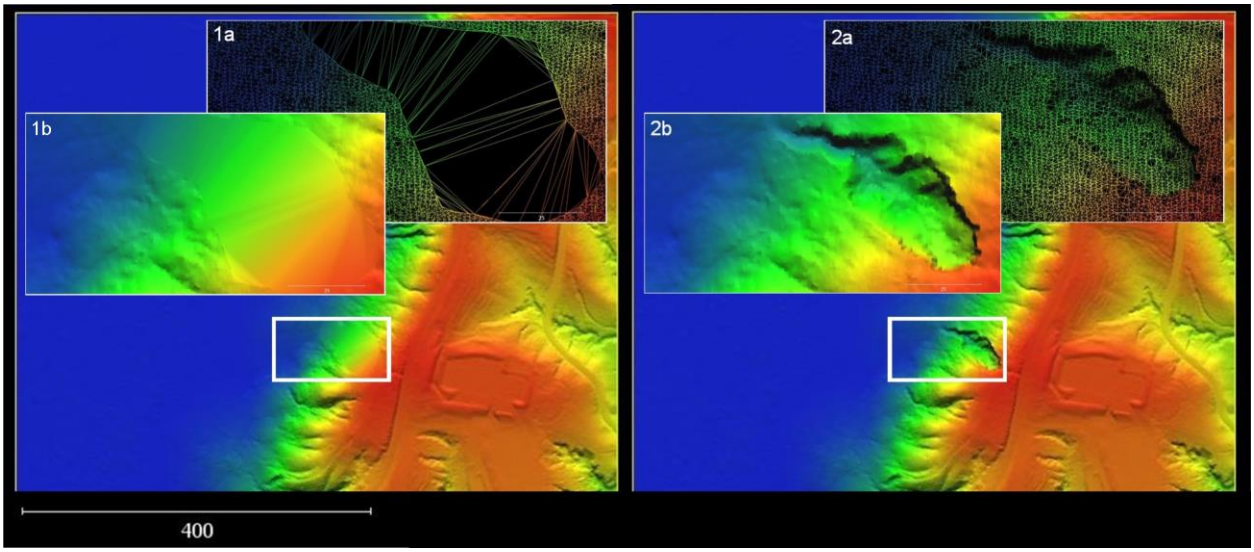



Figure 13. Left: A terrain mesh representing the undisturbed river terrace slope (circa 1970) and surrounding area was produced from the airborne LIDAR point cloud. Inset 1a shows the triangulated mesh produced from terrain points and 1b shows the same mesh colored by elevation. Right: A terrain mesh produced from the terrain points in the airborne LIDAR point cloud. Inset 2a shows the triangulated mesh and 2b shows the same mesh colored by elevation.

Considering that the drainage pipe is comprised of 10 foot segments and the original discharge point was approximately 25 m from its current position, we estimate that three pipe segments lie buried beneath eroded material within the pool valley. This distance indicates an average half meter of headwall retreat per year over the nearly 40 years since the pool was constructed. The change in length of the exposed drainage pipe from its end to its base at the headwall was also measured from the two TLS point clouds to estimate headwall recession over the 49 day period. TLS1 and TLS2 contain 0.82 m and 0.90 m of exposed pipe, respectively. This indicates that the area of headwall immediately surrounding the pipe advanced about 0.08 m over the 49 day period. The detected retreat likely occurred as undercutting caused portions of the headwall to collapse, evidenced by large chunks of headwall material at its base (Figure 1, Appendix III). Soil erosion and mass wasting of the southeast-facing headwall of the gully is visually evidenced by segments of the pipe falling to the valley bottom. One such pipe segment is seen in photos in Figure 2 of Appendix III that were taken on the days of the two TLS surveys. The pool gully headwall erosion is of a critical concern to park management as it approaches a nearby access road.

The DEM produced from the ALS point cloud in 2012 was also compared to the DEMs of comparable resolution (0.66 m) produced from the TLS1 and TLS2 point clouds to quantify change volume for the *gully channel* area of interest. During the roughly 3-year period between the ALS survey (1/24/2012) and the first of the two TLS surveys (12/25/2014), the volume of eroded material was estimated to be 615.8 $m^3$. The volume of eroded material was estimated to be 616.9 $m^3$ between the ALS survey (1/24/2012) and the second of the two TLS surveys (2/8/2015), indicating that an additional 1.1 $m^3$ of material was eroded during the 49 days between TLS1 and TLS2 (12/25/2014 - 2/8/2015). The comparisons are summarized in Table 4.

Table 4. Summary of volumes of change from differencing the digital elevation models from each terrestrial LIDAR survey (here, TLS) with the digital elevation models from the airborne LIDAR survey (here, ALS)

| Model comparison | Resolution ($m^2$) | Area of Interest | Volume Eroded ($m^3$) |
|---|---|---|---|
| $DEM_{1969:1973} - DEM_{ALS\ 2012}$ | 0.4356 | Entire gully | 9985.9 |
| $DEM_{ALS} - DEM_{TLS1}$ | 0.4356 | Gully channel | 615.8 |
| $DEM_{ALS} - DEM_{TLS2}$ | 0.4356 | Gully channel | 616.9 |

To investigate the detailed changes of erosion and deposition within the *gully channel* area of interest, the volume change between TLS1 and TLS2 was calculated using DEMs of 0.02 m. The total volume change within the gully channel over the 49 day period between December 2014 and February 2015 is -2.1 $m^3$, indicating a net import of material into the gully channel. The volume of change consists of 13.6 m of gross deposition and 11.5 m of gross erosion. Figure 14 depicts the ΔDEM from the gully channel in three dimensions. The red to blue color gradient represents the spectrum from net erosion to net deposition.

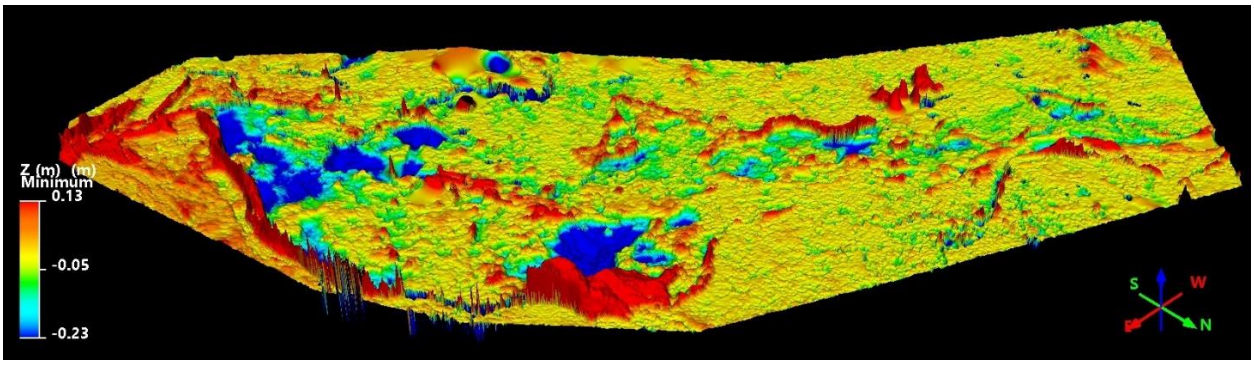



Figure 14. Difference model of the *gully channel* created by calculating the volume difference between the digital elevation models produced from the two terrestrial LIDAR surveys. The change detected for the two sub-areas (*gully head* and *left wall*) with respect to the rest of the gully channel is clearly depicted. Erosion and deposition are shown in red and blue, respectively, contrasting the yellow and green that represent relatively stable portions of the *gully channel*.

The two areas of interest within the *gully channel* contain a large proportion of the cells that represent either tail of the distribution of ΔDEM values. The *gully head* area covers 97 $m^2$ directly beneath the pipe with an average slope of 35.3 degrees. The volumes of 3.5 $m^3$ of gross deposition and 2.6 $m^3$ of gross erosion account for 25.7% and 22.6% of the respective total for each for the study area within the *gully channel*. The *left wall* covers approximately 80 $m^2$ of surface area of the northern sidewall of the pool valley with an inward slope around 48 degrees. We measured approximately 2.5 $m^3$ gross deposition and 3.6 $m^3$ of gross erosion at the left wall, or 18.3% and 31.3% of the respective total for each. The change detected for these two sub-areas with respect to the rest of the gully channel is clearly depicted in Figure 14. The two areas of erosion and deposition are shown in red and blue, respectively, contrasting the yellow and green that represent the relatively stable portions of the channel.

## 5.2 Scale analysis

A total of 64 additional DEMs of the *gully channel* were produced in 0.02 m cell dimension increments from 0.02 m to 0.66 m from resampled TLS point clouds. Statistics summarizing the basic parameters for each DEM are listed in Tables A1 and A2 of the appended materials. The quantities of erosion and deposition measured at the incremental resolutions revealed minor variations in volume measurements with each reduction in DEM resolution until approximately 0.30 m. A summary of the volumes of change at the various resolutions are included in Table 5 and illustrated in the plots in Figure 16.

Table 5. Volume calculations digital elevation models (DEMs) produced from the initial terrestrial LIDAR survey of TLS1 above (deposition) and below (erosion) DEMs from the follow-up terrestrial LIDAR survey.

| Resolution (m) | Volume Erosion ($m^3$) | Volume Deposition ($m^3$) |
|---|---|---|
| 0.02 | 11.5 | 13.6 |
| 0.04 | 11.4 | 13.5 |
| 0.06 | 11.3 | 13.4 |
| 0.08 | 11.3 | 13.3 |
| 0.10 | 11.4 | 13.5 |
| 0.12 | 11.2 | 13.5 |
| 0.14 | 11.3 | 13.3 |
| 0.16 | 11.3 | 13.5 |
| 0.18 | 11.3 | 13.7 |
| 0.20 | 11.4 | 13.6 |
| 0.22 | 11.6 | 13.5 |
| 0.24 | 11.4 | 13.5 |
| 0.26 | 11.6 | 13.9 |
| 0.28 | 11.9 | 14.3 |
| 0.30 | 11.9 | 14.7 |
| 0.32 | 11.7 | 14.8 |
| 0.34 | 12.2 | 15.3 |
| 0.36 | 11.9 | 15.4 |
| 0.38 | 12.4 | 15.5 |
| 0.40 | 12.5 | 15.9 |
| 0.42 | 12.7 | 15.7 |
| 0.44 | 12.5 | 16.0 |
| 0.46 | 12.3 | 15.8 |
| 0.48 | 12.8 | 16.8 |
| 0.50 | 13.3 | 16.4 |
| 0.52 | 13.1 | 16.0 |
| 0.54 | 12.4 | 16.9 |
| 0.56 | 12.5 | 17.0 |
| 0.58 | 13.5 | 17.2 |
| 0.60 | 13.2 | 17.7 |
| 0.62 | 13.4 | 17.5 |
| 0.64 | 13.3 | 17.1 |
| 0.66 | 14.0 | 17.4 |

The mean, maximum, and minimum volumes of erosion calculated from models between 0.02 and 0.30 m resolution are 11.5 $m^3$, 11.9 $m^3$, and 11.2 $m^3$, respectively. After 0.30 m, measured volumes of erosion increase towards the maximum 14.0 $m^3$ measured from the 0.66 m resolution ΔDEM. The mean, maximum, and minimum volumes of deposition calculated from models between 0.02 and 0.30 m resolution are 13.7 $m^3$, 14.7 $m^3$, and 13.3 $m^3$, respectively. After 0.30 m, measured volumes of deposition increase and generally become more variable. We can expect the segmented regression analysis to reveal thresholds at resolutions near the onset of the increasing measurements for erosion and deposition.

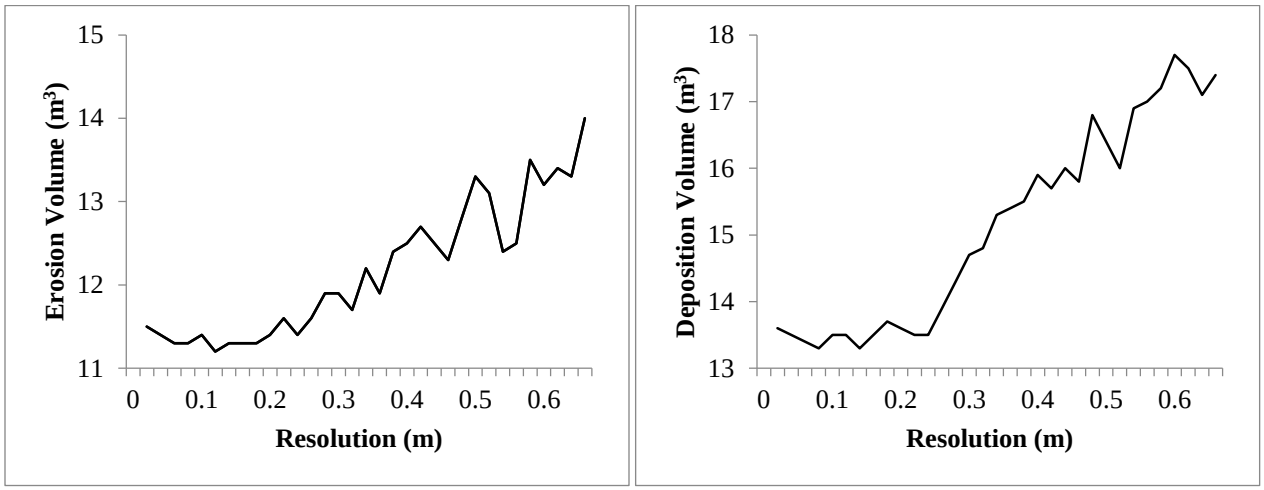



Figure 16. Erosion and deposition measurements from the differenced elevation models from the two terrestrial LIDAR surveys ($DEM_{TLS1} - DEM_{TLS2} = \Delta DEM$) at resolutions between 0.02 m 0.66 m. Treating the 0.02 m difference models as reference, volumes of erosion and deposition are increasingly overestimated with decreasing resolution. The corresponding data is located in Table 5.

The strength of the fit for each break point in the iterative segmented regression analysis was evaluated by its MSE. The MSE for the fits at each break point from 0.1 m to 0.56 m are listed in Table 3 of Appendix I and plotted in Figure 17. The lowest residual MSE for the erosion

and deposition measurements indicate break points at exist 0.18 m (MSE=0.2490) and 0.28 m (MSE=0.2516) resolutions, respectively.

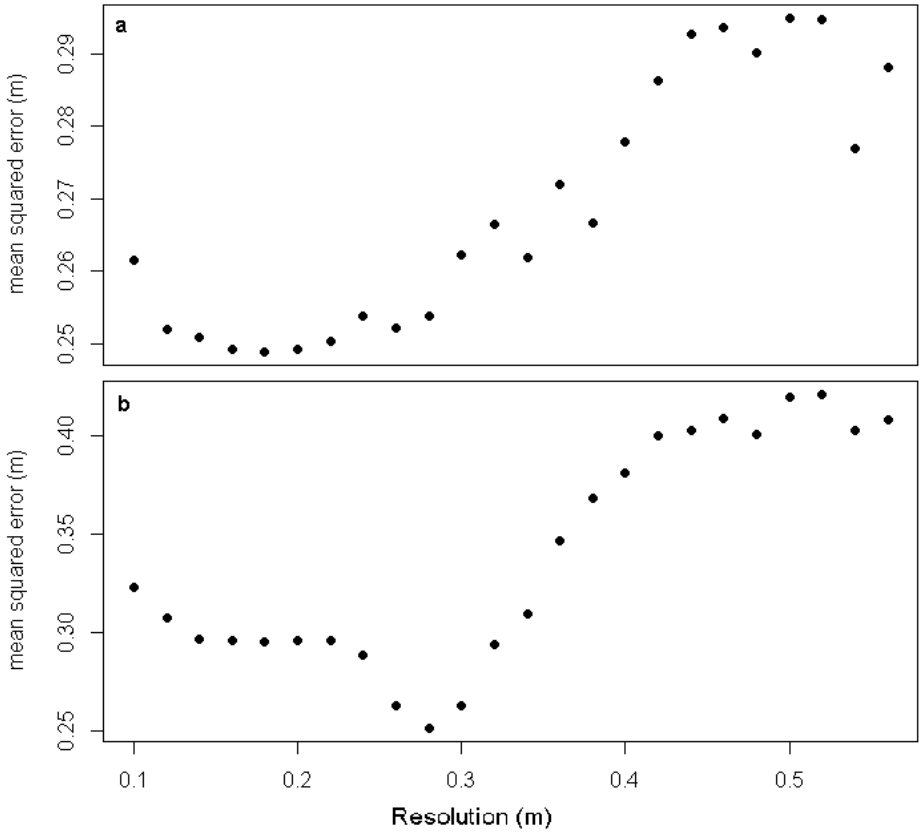



Figure 17. a) Mean square errors (m) for segmented regression lines fit to erosion measurements at each break point; b) Mean square errors (m) for segmented regression lines fit to deposition measurements at each break point. The corresponding data is located in Table 3 of Appendix I.

The patterns of computed MSEs for erosion and deposition indicate that variation in measured volumes of both increase as resolution decreases. The lowest MSE of the regressions for erosion measurements (break point = 0.18 m resolution) reveals some interesting information about the measurements at the resolutions above and below. When DEM resolution is less than 0.18, the linear fit of erosion volume measurements by resolution is given by the equation:

$y = -1.00x + 11.43$ ($p= 0.06$)

Relatively low $R^2$ value ($R^2= 0.40$) indicates that the decreasing resolution is not strongly associated with the minor decrease exhibited in the measured erosion volumes down to the break point resolution. When model resolution is greater than 0.18, the linear fit of erosion volume measurements by resolution is given by the equation:

$y = -4.76x + 10.43$ ($p= 1.15E-11$)

The low p-value indicates that the regression is statistical significance. The high $R^2$ value ($R^2= 0.87$) indicates that the apparent increase in volumes of erosion measured after the break point is strongly associated with decreasing resolution. The two regressions indicate that resolution has very little, if any, effect on volumes of erosion measured from 0.18 m or finer DEMs, while DEMs of resolutions greater than 0.18 increasingly overestimate erosion volumes. The two linear fits for erosion are illustrated in the plot in Figure 18.

The lowest MSE for the segmented regressions of deposition volume by resolution indicate a break point at 0.28 m resolution. Visual interpretation of the plotted deposition volumes by resolution (Figure 16) suggest that the true break point is closer to 0.24 m resolution. A segmented regression was fit to a break point at 0.24 m resolution for deposition volume measurements by resolution. When DEM resolution is less than 0.24, the linear fit of erosion volume measurements by resolution is given by the equation:

$y = 0.37x + 13.144$ ($p= 0.48$)

The high p-value indicates that the regression is not statistical significance. The low $R^2$ value ($R^2= 0.05$) indicates that the variation in deposition volume is not related to DEM resolution

through the break point of 0.24 m. When DEM resolution is greater than 0.24 m, the linear fit of deposition volume measurements by resolution is given by the equation:

$y = 8.88x + 11.95$ ($p = 1.05E\text{-}12$)

The low p-value indicates that the regression is statistical significance. The high $R^2$ value ($R^2 = 0.92$) indicates that the apparent increase in volumes of deposition measured after the break point is strongly associated with decreasing resolution. The segmented regression of deposition volume by resolution indicates that deposition is increasingly overestimated with decreasing resolution after the break point at 0.24 m. The two linear fits for deposition are illustrated in the plot in Figure 18.

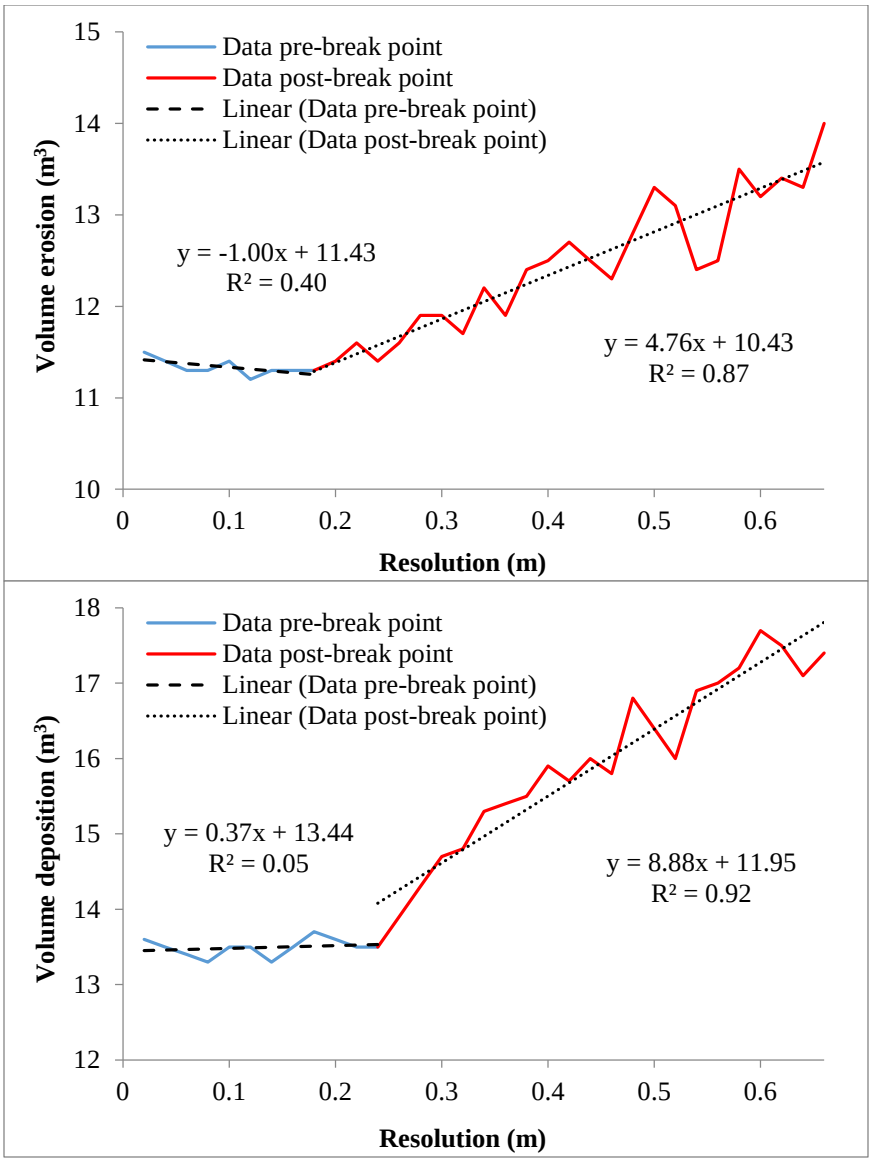



Figure 18. The strongest fits of the segmented regressions for erosion and deposition. Top: The two regressions indicate that resolution has very little, if any, effect on volumes of erosion measured from 0.18 m or higher DEMs, while DEMs of resolutions greater than 0.18 increasingly overestimate erosion volumes. Bottom: The segmented regression of deposition volume by resolution indicates that deposition is increasingly overestimated with decreasing resolution after the break point at 0.24 m.

# CHAPTER SIX

# Discussion

## 6.1 Gully morphometrics

### *6.1.1 ALS-derived gully morphology accuracy and uncertainty*

While subject to uncertainty from a number of assumptions, the estimate of headwall retreat is valuable to park officials concerned by encroachment of the pool gully upon the nearby pool access road. A primary source of potential error is the reliability of registration between the ALS and TLS data for comparison. The ALS point data in the area of the pool valley produced a 0.66 m resolution DEM of the source data set. The relatively sparse distribution of points within the pool valley and pool gully channel is due in part to poor penetration of the dense forest canopy and slope of the valley walls exceeding 20°. Studies have shown that ALS data does not well-represent gullies with slopes greater than 20° and narrow channels (James et al., 2007). The terrain interpolation method often leads to representation of gullies as narrow and steep-sided gullies to appear to have rounded edges and shallow channels, giving an exaggerated appearance of stability (James et al., 2007).

The horizontal margin of error exceeding 0.5 m and vertical margin of error of nearly 0.16 m for points in the ALS point cloud can also have significant impact on volumetric calculations such as those used to measure soil redistribution within the pool gully. Previous investigations indicate that the uncertainty of volume calculations between two DEMs is greater than the nominal error within the original DEMs (Brown and Arbogast, 1999). Woolard and Colby (2002) used ALS-derived DEMs to calculate volumetric change in dunes along the coast of Cape Hatteras, North Carolina, at resolutions ranging from 1 to 20 m. Changes in dune

topography were captured most accurately by comparison of DEMs with resolutions between 1 and 2 m, but calculated error was consistently greater than nominal elevation error within input DEMs. Comparisons of DEMs produced from multi-temporal ALS surveys have demonstrated a tendency to underestimate change volume in areas of complex topography (Heritage and Hetherington, 2007). Furthermore, studies have shown that advertised margins of error often underestimate true vertical and horizontal inaccuracies within ALS datasets (Baltsavias, 1999). A vertical precision lower than that reported by the ALS instrument manufacturer was shown in a survey of an area of the Green River in Utah where authors calculated a mean vertical error of 43 cm for an area of complex topography using a system with a reported uncertainty between 15 and 20 cm (Bowen and Waltermire, 2007).

Another potential error in our calculations is the co-registration of the ALS and TLS data. Inherent differences in the two types point cloud data (ALS and TLS) limit the effectiveness of visual and automated co-registration methods (Tao and Huang, 2014). The Iterative Closest Point (ICP) algorithm is a common method for registering point clouds of similar densities. The ICP chooses the closest pair of points within the two clouds and iteratively transforms the moving cloud to minimize the mean square error until a minimum threshold distance between the two is met (Besl, 1992). Performance of the ICP algorithm has been shown to decrease with increasing complexity of the input point clouds (Gressin et al., 2012) and the ability of RMSE to represent registration accuracy diminishes with increased disparity in point densities (Besl, 1992).

Differences in perspective and coverage, as well as the disparity in positional accuracy of points collected by ALS and TLS systems may affect the estimate of the retreat of the pool valley headwall. The manufacturer produced estimate of horizontal accuracy of the ALS system is between 0.07 and 0.64 (Woolpert, 2011), far less than the range accuracy of the TLS system

(0.002 m) used in this study. Additionally, ALS systems capture points from a top-down perspective over large areas, while TLS systems capture points from an oblique perspective in adjustable fields of view. The greatest detail within an ALS data set occurs at surfaces that face upward and the least detail at surfaces perpendicular to the ground. The opposite is true for TLS systems (Hohenthal et al., 2011; Cheng et al., 2013). A terrestrial LIDAR scanner obtains points from a low perspective and limited vertical FOV such that the tops of surfaces aren't captured directly beneath the scanner and at elevations above the scanner position (Cheng et al., 2013). Another source of difficulty to integrate the two types is the disparity in point density. ALS data is acquired from significantly further distances than TLS data, and thus, relatively few points per unit area are captured (Wu et al., 2010). Registration methods such as the ICP which seek to match pairs of points perform poorly when asked to match many points from the higher density cloud to a single point in the lower density cloud. In addition, automated registration methods often fail to detect corresponding points within discrete point cloud data (Wu et al., 2010; Cheng et al., 2013).

Our attempt to minimize registration error between the ALS and TLS data used in this analysis mimicked the methods used by Cheng et al. (2013) where registration was performed by identifying static features in the ALS point clouds and scanning them with the TLS to ensure corresponding control points existed between the two datasets. By performing scans of the area in the immediate vicinity of the pool, we were able to use three utility poles and the corners of the pool and a nearby building as control points to align the TLS2 cloud to the ALS cloud with an RMSE of 0.21 m. According to registration standards suggested by the American Society for Photogrammetry and Remote Sensing, our RMSE corresponds to an average horizontal accuracy within 15 cm and vertical accuracy within 20 cm (Smith et al., 2014), although RMSE tends to

be overestimated for clouds with highly disparate point densities (Sanii, 2008). The RMSE metric also tends to be less conclusive with regards to accuracy for points that lie farthest away from the control points (Csanyi and Toth, 2007) as is the case with the TLS data collected within the pool valley. The pool valley is located west of the control points used to co-register the ALS and TLS point clouds. In an ideal scenario control points would be well-distributed around the pool valley and yield an RMSE that better represents true co-registration accuracy for points within the pool valley.

### *6.1.2 TLS-derived gully morphology*

Visual interpretation of the ΔDEM produced from the TLS1 and TLS2 survey DEMs suggest that much of the observed volume change is from mass wasting of the gully headwall and sidewalls with steep slopes. Figure 19 depicts a segment of the gully point cloud from TLS2 with points colorized by elevation, slope, and vertical difference as well as a 3D surface model with elevation texture overlay. The areas of warm colors in (c) the vertical difference cloud indicate material eroded between TLS1 and TLS2 and generally coincide with the areas of warm colors in (b) the slope cloud. Also evident in the vertical difference cloud are areas of deposition indicated by the cool colors that are predominately located within the gully channel directly beneath the eroded areas. These are examples of the localized wasting that is characteristic of active gullies described by Imeson and Kwaad (1980). The wasting is likely a repeating cycle of activity exhibited by gullies where collapse of the head- and sidewalls leads to temporary local stabilization and an excess of soil material that is gradually expelled from the channel (Bennett, 1928; Ireland et al., 1939; Morgan, 1996).

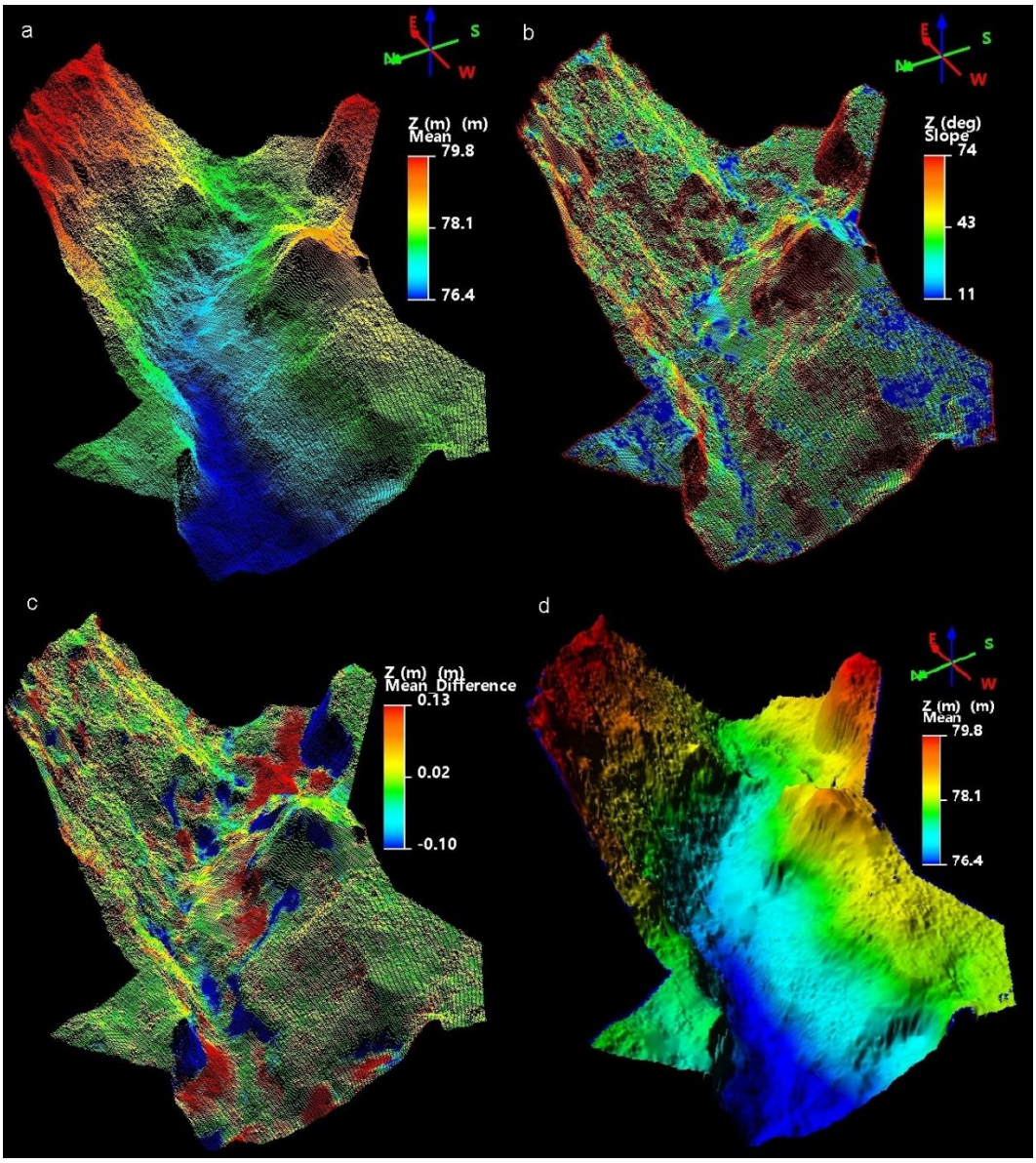



Figure 19. a) Gully point cloud from TLS2 with points colorized by elevation; b) colorized by slope; c) colorized by vertical difference from TLS1; d) interpolated surface colorized by elevation

The pattern of mass wasting is more easily perceived through the cross-sectional plot in the gully channel (Figure 20). Three 4 m wide cross sections 4 m apart and covering a 12 meter length of the *gully channel* extending from the *gully head* to the *left wall* were sampled at 0.02 m resolution from both of the TLS surveys. The solid and dashed lines represent TLS1 and TLS2,

respectively. Cross section pair 1 (TLS1_CS1, TLS2_CS1) shows heavy incising of the gully at the center of the channel. Wasting of the right side wall is also evident as TLS2_CS1 moves up the x axis from the center of the channel. It briefly extends above and then dips back beneath TLS1_CS1 between the 2.7 and 3.2 m portion of the cross section. This half meter section clearly depicts sidewall wasting and the accumulation beneath. Similar wasting is evident in cross section pair 2 between 0.80 m and 1.70 m of the left sidewall and the entire extent of the right sidewall. Incision at the channel center is also apparent although it is not to the same degree as cross section pair 1.

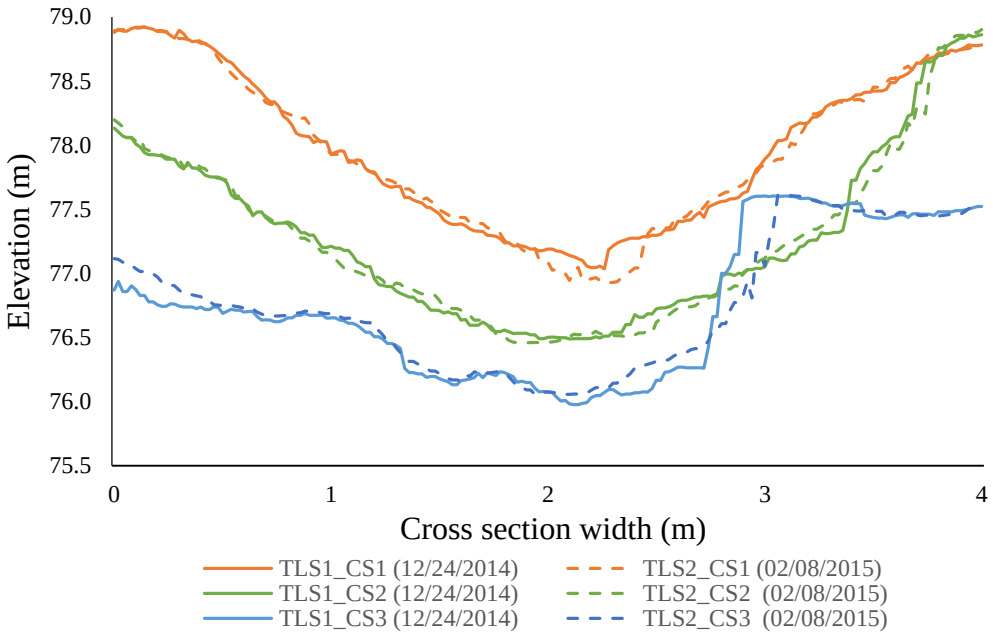



Figure 20. 4 m wide cross sections at 4 m intervals of a 12 m section of the gully channel sampled at 0.02 m resolution. The solid lines are cross sections from the terrestrial LIDAR survey on 12/24/2014 and dashed lines are cross sections from the survey on 02/08/2015.

Cross section pair 3 shows substantial deposition of material at the base of the right sidewall between 2.04 m and 2.76 m. TLS1_CS3 shows a near-vertical right sidewall that appears to have retreated approximately 18 cm at its peak when compared to TLS2_CS3.

These cross sections are likely snapshots of repeating phases of gully channel dynamics described in published literature. Cross section pair 1 shows a phase of relative stability characterized by gently sloping sidewalls with rounded upper edges and the majority of erosion activity occurring in the center of the channel (Heede, 1976; Morgan 1996; Bull and Kirkby, 1997). Over time we can expect further incision of the channel bed and erosion at the base of the sidewalls, increasing their slope, decreasing their stability, and widening their upper edges (Bocco, 1991; Morgan, 1996). Cross section pair 2 shows moderate degrees of sidewall activity and channel incision. The right sidewall is steeply sloped and alternates between areas of erosion and deposition to its peak while the left sidewall has reached relative stability comparable to that of the sidewalls in cross section pair 1. The imbalance between the left and right sidewalls is a feature of the migrating gully channel (Bocco, 1991) as it widens disproportionately in one direction before reversing and widening in the other direction (Imeson and Kwaad, 1980; Bocco, 1991). Cross section pair 3 shows accumulation of material on the left sidewall from portions outside the plot area. The right sidewall is in rapid retreat as this pair of cross sections is in the most unstable phase of widening and infilling (Bocco, 1991; Morgan, 1996).

The volumes measured in this analysis are the aggregated vertical difference of all cells greater- or less-than zero, such that they represent all detectable redistributions of material within the area of observation in the gully. For this reason, adjacent cells with detectable volumes of erosion and deposition may account for the same material. A better representation of the geomorphic processes at play in the gully channel may be to quantify rates of erosion and

deposition, rather than volumes. Future analyses should include bulk density measurements for the active soils so rates and other soil properties calculated per unit area may be established. The TLS measured results should also be validated using erosion pins or similar methods. How local hydrology may be affecting the results is another potential topic to be investigated in the future.

## 6.2 Scale analysis

Both TLS point clouds may contain point densities exceeding that necessary to quantify the gully dynamics. Gallant and Hutchinson (1996) pointed out that the accuracy of derived terrain products is influenced dramatically by DEM resolution. For example, slope gradient exhibits the general tendency to decrease as DEM resolution is decreased (Chang and Tsai, 1991; Thieken et al., 1999; Thompson et al., 2001; Wolock and Price, 1994; Zhang and Montgomery, 1994), and thus, their ability to represent the landscape is diminished at these coarser resolutions. Schoorl et al. (2000) found evidence to suggest that soil loss estimates increased as coarser resolution DEMs were implemented in their statistical model. The similar trend is also observed in our measurements of displaced volume at progressively coarser resolutions. Comparison of field measurements of slope with DEM-derived slope estimates indicate that higher resolution DEMs produce substantially more accurate estimates than lower resolution counterparts (Warren et al., 2004), noting that second-order calculations such as rates of soil erosion and deposition may be impacted heavily by such variation. Research also suggested that high resolution DEMs that are downsampled to resolutions comparable to those of commonly used elevation datasets retain considerably higher detail than DEMs produced from data of equivalent resolution (Vaze et al., 2010). This begs the question of whether the same is true of downsampled LIDAR data. The lower resolution DEMs used in this analysis were produced by downsampling the LIDAR

point clouds and interpolating from the remaining points rather than resampling a 2-dimensional DEM at lower resolution.

The relationship revealed in our results agrees with the generalization that the ability of coarse resolution DEMs to accurately represent the terrain is diminished with increasing topographic relief. Schoorl et al. (2000) found that this effect is reflected in derived volumes of erosion and deposition in their analysis of time series DEMs of modeled catchments. They tested this by calculating rates of erosion and sedimentation using DEMs of 5 different pixel resolutions. The degree to which erosion overestimated increased with each reduction in DEM resolution. The authors also provided evidence that sediment re-deposition increased at finer resolutions, indicating that some over-prediction of erosion measurements may be confounded by diminished ability of coarsened DEMs to capture re-sedimentation (Schoorl et al., 2000). While our erosion volume measurements follow a similar trend to that demonstrated by Schoorl et al. (2000), deposition volume measurements within the pool gully channel did not increase at finer resolution. This opposite trend in our data could be the result of the exceptionally high levels of deposition occurring in the portion of the pool gully in which this research is focused. Our TLS data was gathered in the portion of gully channel nearest the headwall of the pool valley. The gully channel extends a distance beyond the scope of our survey roughly equivalent in length to the segment for which we have data. Imported material into the gully channel may be lower in these further sections because there is less material to potentially collapse into the gully from the shorter sidewalls. This area could perhaps more closely resemble trends in re-sedimentation shown in the artificial catchments used by Schoorl et al. (2000). It is also possible that local relief inside the pool gully channel is significant enough that their trends are not applicable.

The established resolution thresholds for the calculations of erosion (0.18 m) and deposition (0.24 m) volumes provide noteworthy insight into our data and acquisition methods. The gentle slopes of the regression lines fit before the two break points compared with the slopes of the fits after them indicate that the erosion and deposition measurements hold relatively constant at resolutions higher than the break point thresholds. This inference is also supported by the tight distribution of data points before the break point thresholds compared with those after. Two useful pieces of information are gleaned from applying the segmented regression to our data if assuming the highest resolution DEMs most accurately represent the gully terrain: 1) volumes of erosion and deposition within the pool gully measured from DEMs of at least 0.24 m resolution are reasonably close to those measured from the baseline 0.02 m DEMs, and 2) increasingly overestimated volumes of erosion and deposition are derived from the DEMs of resolution lower than 0.18 m and 0.24 m, respectively.

To demonstrate the potential for increased efficiency in TLS data processing by collecting point data of appropriate densities, we can measure the length of time taken to read an ASCII point cloud to a data array in R. The 0.02 m DEM for TLS1 was interpolated from approximately 835,000 terrain points versus approximately 4,250 points for a 0.28 m DEM. Each data point consists of three 32-bit float coordinate values and three 8-bit integer RGB values. R read the two clouds to an array in 2.72 and 0.03 seconds, respectively (Appendix IV), on a 3.1 GHz consumer grade laptop running Windows 10. For comparison, the same operation required 103 seconds for one of the five original, unfiltered point clouds from TLS1 containing approximately 32,000,000 points. Computer resources are truly strained when processing requires that multiple unfiltered clouds (approaching two gigabytes each in the case of the TLS1 point cloud data) be loaded to memory. This exercise illustrates the value that knowledge of

LIDAR data resolution requirements adds for this application moving forward. This knowledge will improve future acquisition and processing of LIDAR data from the pool gully.

# CHAPTER SEVEN

## Conclusions

In this thesis, I calculated volumes of erosion and deposition over two periods within a small gully using multi-temporal airborne and terrestrial LIDAR point cloud data. The data acquired using TLS exceeded the necessary point density to produce DEMs of 2 cm resolution. Differencing DEMs from the two surveys resulted in volumes of gross erosion (11.5 $m^3$) and deposition (13.6 $m^3$) within the *gully channel* that seem reasonable for the period between 12/24/2014 and 02/08/2015. Visual inspection of the ΔDEM suggests that the detected net deposition was likely the result of the wasting head- and side-walls of the larger pool valley into the gully channel. These results indicate that detectable volumes of erosion and deposition occurred within the gully.

The eroded volume measured for the time between the ALS survey and the first of the TLS surveys (615.8 $m^3$; ~2.9 years) agrees with the total volume of displaced material over the period between the pool gully initiation and the ALS survey (9985.9 $m^3$; ~ 42 years). The same is true to a lesser degree for the volume measured for the period between the ALS survey and the second of the TLS surveys (616.9 $m^3$; ~3.0 years). These results raise questions about the method of comparison between the ALS and TLS data because no deposition was detected through either calculation ($DEM_{ALS} - DEM_{TLS1} = \Delta DEM$; $DEM_{ALS} - DEM_{TLS2} = \Delta DEM$) while deposition was detected (17.4 $m^3$) through differencing of the resampled TLS DEMs at resolutions comparable to that of the ALS data set ($DEM_{TLS1\ 0.66m} - DEM_{TLS2\ 0.66m} = \Delta DEM$). The accuracy of the co-registration between the ALS data set and the two TLS data sets is worth further investigation. I hypothesize that the poor spatial distribution of control points used in the co-registration caused

overestimation of the computed RMSE. The man-made features that were used as control points between the ALS and TLS data sets were located no less than 50 meters east of the gully so the accuracy of their alignment is suspect. It is recommended that the RMSE between the ALS and transformed TLS data sets be computed for a sample of points within the gully rather than a sample of points across the entire data sets if the ALS data is to be incorporated in any future analyses.

I also calculated the erosion and deposition volumes from DEMs resampled at a variety of resolutions to identify an optimal point density for data sets used to measure geomorphic changes within the gully. The choice of point density is significant because it is a function of the desired nominal point spacing set by the operator of the TLS instrument in the field. For the purpose of the analysis, it is assumed that the DEMs of 0.02 m resolution provided the most accurate estimation of the gross volumes of erosion and deposition within the pool gully over the 49 day period. The analysis exposed a trend of increased overestimation of volumes of both erosion and deposition at decreased DEM resolutions. The tendency to overestimate erosion with decreases in resolution is exhibited in a similar study by Schoorl et al. (2000). However, the deposition volumes measured by Schoorl et al. (2000) were increasingly underestimated as resolution decreased in their analysis. The opposite trend was observed in the scale analysis presented in this thesis. This is perhaps because the slope in the steepest portions of our study area may be represented by just one or two cells in the lower resolution models (>0.28 m). This can result in cell values that average points representing both the top and bottom of the gully sidewall. One potential improvement to the analysis moving forward would be to make the calculations for the steeper portions of the gully directly from the point clouds. The thresholds established through the segmented regression indicate that the decreases in terrain model

resolution begin to strongly affect the erosion and deposition volume calculations at those thresholds, 0.18 m and 0.28 m resolution for erosion and deposition, respectively. Based on this information, for future surveys of the pool gully the TLS instrument can be set to collect points at densities between 10 and 30 points per square meter to optimize efficiency without diminishing the quality of subsequent analyses.

The erosion and deposition volume measurements may be better assessed by extending the temporal coverage of our point cloud datasets within the gully. Further analysis of the gully through additional TLS surveys will help to validate inferences made from the two observations to date. Coupling these data with in-depth analysis of soil profiles in the gully channel will lend further insight into erosion and deposition processes within the pool gully.

# REFERENCES

Baltsavias, E.P. 1999. A comparison between photogrammetry and laser scanning. *International Society of Photogrammetry and Remote Sensing: Journal of Photogrammetry and Remote Sensing* 54: 83-94.

Bangen, S.G., J.M Wheaton, N. Bouwes, B. Bouwes, and C. Jordan. 2014. A methodological intercomparison of topographic survey techniques for characterizing wadeable streams and rivers. *Geomorphology* 206: 343-361.

Barnhardt, M. 1988. Historical Sedimentation in West Tennessee Gullies. *Southeastern Geographer* 281:18-31.

Barnhardt, M. 1988. Recent gully activity in Meeman-Shelby State Park Southwest Tennessee, USA. *Journal of the Tennessee Academy of Science* 63: 61-64.

Barnhardt, M. 1989. A 50-Year-Old Gully Reclamation Project Revisited. *Journal of Soil and Water Conservation* 44: 562-565.

Bennett, H. H. 1928. The Geographical Relation of Soil Erosion to Land Productivity. *Geographical Review*, 18: 579-605.

Betts, H. D., N.A. Trustrum, and R.C. De Rose. 2003. Geomorphic changes in a complex gully system measured from sequential digital elevation models, and implications for management. *Earth Surface Processes and Landforms* 28: 1043-1058.

Besl, P.J., and N.D. McKay. 1992. A Method for registration of 3-D shape. *Proceedings of the SPIE* 1611: 239-256.

Bocco, G. 1991. Gully Erosion - Processes and Models. *Progress in Physical Geography* 15: 392-406.

Bowen, Z. H., and R.G. Waltermire. 2007. Evaluation of light detection and ranging (LIDAR) for measuring river corridor topography. *Journal of the American Water Resources Association* 38: 33-41.

Brodu, N., and D. Lague. 2012. 3D terrestrial LIDAR data classification of complex natural scenes using a multi-scale dimensionality criterion: Applications in geomorphology. *International Society of Photogrammetry and Remote Sensing: Journal of Photogrammetry and Remote Sensing* 68: 121-134.

Brown, D.G., and A.F. Arbogast. 1999. Digital Photogrammetric change analysis as applied to active coastal dunes in Michigan. *Photogrammetric Engineering and Remote Sensing* 65: 467-474.

Bull, L.J., and M.J. Kirkby. 1997. Gully processes and modelling. *Progress in Physical Geography* 21: 354-374.

Cang, G., M. Li, J. Yue, J. Ou, and L. Zhu. 2013. Effect of Target Properties on Terrestrial Laser Scanning Intensity Data. *Proceedings of the 2013 the International Conference on Remote Sensing, Environment and Transportation Engineering* 31: 818-821.

Carr, S., B. Douglas, and C. Crosby. 2013. Terrestrial Laser Scanning (TLS) Field Camp Manual, UNAVCO, Boulder, Co. 5-7 pp.

Cavalli, M., P. Tarolli, L. Marchi, and G.D. Fontana. 2008. The effectiveness of airborne LIDAR data in the recognition of channel-bed morphology. *Catena* 73: 249-260.

Challis K. 2006. Airborne laser altimetry in alluviated landscapes. *Archaeological Prospection* 13: 103–127. DOI: 10.1002/arp.272

Chang, K.T., and B.W. Tsai. 1991. The Effect of DEM Resolution on Slope and Aspect Mapping. *Cartography and Geographic Information Systems* 18: 69-77.

Charlton, R. 2008. *Fundamentals of Fluvial Geomorphology*. Routledge, New York. 143 pp.

Cheng, L., L. Tong, M. Li, and L. Yongxue. 2013. Semi-Automatic Registration of Airborne and Terrestrial Laser Scanning Data Using Building Corner Matching with Boundaries as Reliability Check. *Remote Sensing* 5: 6260-6283.

Corsini, A., C. Castagnetti, E. Bertacchini, R. Rivola, F. Ronchetti, and A. Capra. 2013. Integrating airborne and multi-temporal long-range terrestrial laser scanning with total station measurements for mapping and monitoring a compound slow moving rock slide. *Earth Surface Processes and Landform*s 38: 1330-1338.

Croke, J., P. Todd, C. Thompson, F. Watson, R. Denham, and G. Khanal. 2013. The use of multi-temporal LIDAR to assess basin-scale erosion and deposition following the catastrophic January 2011 Lockyer flood, SE Queensland, Australia. *Geomorphology* 184: 111-126.

Csanyi, N. and C.K. Toth. 2007. Improvement of LIDAR data accuracy using LIDAR-specific ground targets. *Photogrammetric Engineering and Remote Sensing* 73: 385-396.

Crombe, P. 2013. Application of the topographic position index to heterogeneous landscapes. *Geomorphology* 186: 39-49.

Downes, R.G. 1946. Tunnelling erosion in north-eastern Victoria. *Journal of the Council of Scientific and Industrial Research* 19: 283-292.

Deng Y., J.P. Wilson, and B.O. Bauer. 2007. DEM resolution dependencies of terrain attributes across a landscape. *International Journal of Geographical Information Science*, 21 (2): 187-213.

Endale, D.M., H.H. Schomberg, and J.L. Steiner. 2000. Long Term Sediment Yield and Mitigation in a Small Southern Piedmont Watershed. *International Journal of Sediment Research* 14: 60-68.

Farr, T.G., P.A. Rosen, E. Caro, R. Crippen, R. Duren, S. Hensley, M. Kobrick, M. Paller, E. Rodriguez, L. Roth, D. Seal, S. Shaffer, J. Shimada, and J. Umland. 2007. The Shuttle Radar Topography Mission. *Rev. Geophys.* 45: RG2004, doi:10.1029/2005RG000183.

Faro Scene 5.3.3. 2015. Faro Technologies, Lake Mary, Florida, USA; <http://www.faro.com>

Federal Geographic Data Committee. 1998. *Geospatial Positioning Accuracy Standards Part 3: National Standard for Spatial Data Accuracy*. FGDC-STD-007.3-1998.

Gesch, D.B., M.J. Oimoen, and G.A. Evans. 2014. Accuracy assessment of the U.S. Geological Survey National Elevation Dataset, and comparison with other large-area elevation datasets—SRTM and ASTER: U.S. Geological Survey Open-File Report 2014–1008, 10 p., http://dx.doi.org/10.3133/ofr20141008.

Gressin, A., C. Mallet, and N. David. 2012. Improving 3D LIDAR point cloud registration using optimal neighborhood knowledge. *International Society for Photogrammetry and Remote Sensing: Annals of the Photogrammetry, Remote Sensing and Spatial Information Sciences* 1-3: 111-116.

Guisan, A., S.B. Weiss, and A.D. Weiss. 1999. GLM versus CCA spatial modeling of plant species distribution. *Plant Ecology* 143: 107-122.

Heede, B.H., Rocky Mountain Forest and Range Experiment Station (Fort Collins Colo.), & United States. Forest Service. 1976. Gully development and control: the status of our knowledge. Fort Collins, Colo.: Dept. of Agriculture, Forest Service, Rocky Mountain Forest and Range Experiment Station.

Heritage, G., and D. Hetherington. 2007. Towards a protocol for laser scanning in fluvial geomorphology. *Earth Surface Processes and Landforms* 32: 66-74.

Heritage, G. L., D.J. Milan, A.R.G. Large, and I.C. Fuller. 2009. Influence of survey strategy and interpolation model on DEM quality. *Geomorphology* 112: 334-344.

Hilker, T.H., N.C. Coops, G.J. Newnham, M. van Leeuwen, M.A. Mulder, J.D. Stewart, and D.S. Culvenor. 2012. Comparison of Terrestrial and Airborne LIDAR in Describing Stand Structure of a Thinned Lodgepole Pine Forest, *Journal of Forestry* 10: 97-104.

Hodge, R., J. Brasington, and K. Richards. 2009. In situ characterization of grain-scale fluvial morphology using Terrestrial Laser Scanning. *Earth Surface Processes and Landforms* 34: 954-968.

Hofle, B., L. Griesbaum, and M. Forbriger. 2013. GIS-Based Detection of Gullies in Terrestrial LIDAR Data of the Cerro Llamoca Peatland (Peru), *Remote Sensing*, 5: 5851-5870.

Hohenthal, J., P. Alho, J. Hyyppa, and H. Hyyppa. 2011. Laser scanning applications in fluvial studies. *Progress in Physical Geography* 35: 782-809.

Huaxing B., L. Xiaoyin, G. Mengxia, L. Xin, and L. Jun. 2006. Digital terrain analysis based on DEM. *Frontiers of Forestry in China* 1: 54-58.

Hudson, N. 1981. *Soil conservation (2nd Edition).* Cornell University Press, New York. 24-56 pp.

Imeson, A.C., and F.J.P.M. Kwaad. 1980. Gully types and gully prediction. *Geografisch Tijdschrift* 14: 430-441.

Ireland, H.A., C.F.S. Sharpe, and D. Eargle. 1939. Principles of gully erosion in the Piedmont of South Carolina. U.S. Dept. of Agriculture, Washington D.C.

James, L.A., D.G. Watson, and W.F. Hansen. 2007. Using LIDAR data to map gullies and headwater streams under forest canopy: South Carolina, USA. *Catena* 71: 132-144.

Kaasalainen, S., A. Jaakkola, M. Kaasalainen, A. Krooks, and A. Kukko. 2011. Analysis of Incidence Angle and Distance Effects on Terrestrial Laser Scanner Intensity: Search for Correction Methods. *Remote Sensing* 31: 2207-2221.

Knighton, D. 1998. *Fluvial Forms & Processes: A New Perspective.* Arnold, London. 135 pp.

Kukko, A., S. Kaasalainen, and P. Litkey. 2008. Effect of incidence angle on laser scanner intensity and surface data. *Applied Optics* 47: 986-992.

Lohani, B., and D.C. Mason. 2001. Application of airborne scanning laser altimetry to the study of tidal channel geomorphology. *ISPRS Journal of Photogrammetry and Remote Sensing* 56: 100–120. DOI: 10.1016/S0924-2716(01)00041-7

Leopold, L.B., and J.P. Miller. 1956. Ephemeral streams: hydraulic factors and their relation to the drainage net. Washington: U.S. Govt. Print.

Marks, K., and P. Bates. 2000. Integration of high-resolution topographic data with floodplain flow models. *Hydrological Processes* 14: 2109-2122.

McKean J., and J. Roering. 2004. Objective landslide detection and surface morphology mapping sing high-resolution airborne laser altimetry. *Geomorphology* 57: 331-351.

Milan, D.J., G.L. Heritage, D. Hetherington. 2007. Application of a 3D laser scanner in the assessment of erosion and deposition volumes and channel change in a proglacial river. *Earth Surface Processes and Landforms* 32: 1657-1674.

Morgan, R.P.C. 1979. *Soil erosion.* Longman, New York.

Morgan, R.P.C. 1996. *Soil erosion and conservation (2nd edition*). Longman, Harlow. 213 pp.

Neter, J., W. Wasserman, and M.H. Kutner. 1990. *Applied Linear Statistical Models, 3nd ed.* Burr Ridge, IL: Irwin. 1181 p.

Notebaert, B., G. Verstraeten, G. Govers, and J. Poesen. 2008. Qualitative and quantitative applications of LIDAR imagery in fluvial geomorphology. *Earth Surface Processes and Landforms* 34: 217-321.

Nutter, W.L., and J.E. Douglass. 1978. Consequences of Harvesting and Site Preparation in the Piedmont, Symposium on Principles of Maintaining Productivity on Prepared Sites, Mississippi State University, 1977.

Perroy, R., B. Bookhagen, G. Asner, and O. Chadwick. 2010. Comparison of gully erosion estimates using airborne and ground-based LIDAR. *Geomorphology* 118: 288-300.

Picco, L., L. Mao, M. Cavalli, E. Buzzi, R. Rainato, and M.A. Lenzi. 2013. Evaluating short-term morphological changes in a gravel-bed braided river using terrestrial laser scanner. *Geomorphology* 201: 323-334.

Poesen, J. 1993. Gully topology and gully control measures in the European loess belt. In: Wicherek, S. (Ed.), *Farm Land Erosion in Temperate Plains Environment and Hills*. Elsevier, Amsterdam, pp. 221-239

Poesen, J., J. Nachtergaele, G. Verstraeten, and C. Valentin. 2003. Gully erosion and environmental change: importance and research needs. *Catena* 50: 91-133.

Poesen, J., K. Vandaele, and B. Van Wesemael. 1998. Gully erosion: importance and model implications. In: Boardman, J., Favis-Mortlock, D.T. (Eds.), Modeling Soil Erosion by Water. Springer, Berlin, pp. 285-311.

Poesen, J., T. Vanwalleghem, J. de Vente, A. Knapen, G. Verstraete, and J.A. Martinex-Casasnovas. 2006. Gully erosion in Europe. In: Boardman, J., Poesen, J. (Eds.), Soil Erosion in Europe. Wiley, Chichester, pp. 515-536.

Pool and Spa, The Basics of Swimming Pool Filters, Web page, accessed 13 April, 2016 at http://www.poolandspa.com/page799.htm.

Ryan, S.E. and L.S. Porth, 2007. A Tutorial on the Piecewise Regression Approach Applied to Bedload Transport Data, United States Department of Agriculture Forest Service General Technical Report RMRS-GTR-189, May 2007.

Rumsby, B.T., J. Brasington, J.A. Langham, S.J. McLelland, R. Middleton, and G. Rollinson. 2008. Monitoring and modelling particle and reach-scale morphological change in gravel-bed rivers: Applications and challenges. *Geomorphology* 93: 40-54.

Samberg, A. 2005. Geospatial Positioning Accuracy Standards: National Standard for Spatial Data Accuracy, Federal Geographic Data Committee. 7 pp.

Sanii, S. 2008. *Assessing the effect of point density and terrain complexity on the quality of LIDAR-derived DEMs in multiple resolutions*. M.S. Thesis, University of Calgary.

Schoorl, J.M., M.P.W. Sonneveld, and A. Veldkamp. 2000. Three-Dimensional Landscape Process Modelling: The Effect of DEM Resolution. *Earth Surface Processes and Landforms* 25: 1025-1034.

Smith, D.L., L.N. Graham, D.F. Maune, Q.A. Abdullah, H.K. Heidemann, G.Y.G. Lee, and C.K. Sorenson, R., and J. Seibert. 2007. Effects of DEM resolution on the calculation of topographical indices: TWI and its components. *Journal of Hydrology* 347: 79-89.

Tao, T.A., and S.H. Huang. 2014. Surface-Based Registration of Airborne and Terrestrial Mobile LIDAR Point Clouds. *Remote Sensing* 6: 12686-12707.

Tennessee State Parks 2016, Tennessee Department of Environment & Conservation, accessed 9 March 2016, < http://tnstateparks.com/parks/about/meeman-shelby>

Thieken, A.H., A. Lucke, B. Diekkruger, and O. Richter. 1999. Scaling input data by GIS for hydrological modelling. *Hydrological Processes* 13: 611-630.

Thompson, J.A., J.C. Bell, and C.A. Butler. 2001. Digital elevation model resolution: effects on terrain attribute calculation and quantitative soil-landscape modeling. *Geoderma* 100: 67-89.

Toms, J.D., and M.L. Lesperance. 2003. Piecewise regression: A tool for identifying ecological thresholds, *Ecology* 84: 2034-2041.

Toth, C.K. 2014. ASPRS Positional Accuracy Standards for Digital Geospatial Data. *Photogrammetric Engineering and Remote Sensing* 81: A1-A26.

Trimble, S.W. 1974. Man-Induced Soil Erosion on the Southern Piedmont: 1700-1970: Soil Conservation Society of America.

Trimble, S.W. 1985. Perspectives on the History of Soil Erosion Control in the Eastern United States. *Agricultural History* 59: 162-180.

US Climate Data 2016, U.S. Weather Service, accessed 9 March 2016, <http://www.usclimatedata.com>

U.S. Geological Survey (2006), Shuttle Radar Topography Mission, Version 2.0, Global Land Cover Facility, University of Maryland, College Park, Maryland, February 2000.

U.S. Geological Survey, The National Map, 2015, 3DEP products and services: The National Map, 3D Elevation Program Web page, accessed 23 November, 2014 at http://nationalmap.gov/3dep_prodserv.html.

Vittorini, S. 1972. The effect of soil erosion in an experimental station in the Pliocene clay of the Val d'Era (Tuscany) and its influence on the evolution of the slopes. *Acta Geographica Debrecina* 10: 71-81.

Wagner, W., A. Ullrich, V. Ducic, T. Melzer, and N. Studnicka. 2006. Gaussian decomposition and calibration of a novel small-footprint full-waveform digitising airborne laser scanner. *International Society of Photogrammetry and Remote Sensing: Journal of Photogrammetry and Remote Sensing* 60: 100-112.

Weiss, A.D. 2001. Topographic position and landforms analysis. ESRI Users Conference, San Diego, CA.

Wolff, Christian. "The Radar Range Equation." RadarTutorial.eu. Published under Creative Commons Attribution-Share Alike 3.0 Unported license, n.d. Web. 13 March 2016.

Wolock, D.M., and C.V. Price. 1994. Effects of digital elevation model map scale and data resolution on a topography-based watershed model. *Water Resources Research* 30: 3041-3052.

Woolard, J.W., and J.D. Colby. 2002. Spatial characterization, resolution, and volumetric change of coastal dunes using airborne LIDAR: Cape Hatteras, North Carolina. *Geomorphology* 48: 269-287.

Woolpert, 2012. Airborne LIDAR Task Order Report: Shelby County TN 1M NPS LIDAR/Feature Extract. Dayton, OH.

Yang P., D.P. Ames, N.F. Glenn, and D. Anderson. 2010. Effects of LIDAR derived DEM resolution on hydrographic feature extraction. American Geophysical Union, Fall Meeting 2010.

Young, A.P., M.J. Olsen, N. Driscoll, R.E. Flick, R. Gutierrez, R.T. Guza, E. Johnstone, and F. Kuester. 2010. Comparison of Airborne and Terrestrial LIDAR Estimates of Seacliff

Erosion in Southern California, Photogrammetric Engineering and Remote Sensing 76: 421-427.

Zhang, W., and D.R. Montgomery. 1994. Digital elevation model grid size, landscape representation, and hydrologic simulations. *Water Resources Research* 30: 1019-1028.

Zhu, T.X. 2003. Tunnel development over a 12 year period in a semi-arid catchment of the loess plateau, China. *Earth Surface Processes and Landforms* 28: 507-525.

Zhu, L., Y. Mu, and R. Shi. 2008. Study on the Resolution of Laser Scanning Point Cloud, Proceedings of the IEEE International Geoscience and Remote Sensing Symposium, Boston, 2008.

# APPENDIX

# Appendix I. Tables

Table A1. Elevation statistics of resampled DEMs from the terrestrial LIDAR survey on 12/24/2014

| Cell x,y (m) | Resolution ($m^2$) | Pts | Pts/$m^2$ | Min Z (m) | Max Z (m) | Mean Z (m) | Std Z (m) |
|---|---|---|---|---|---|---|---|
| 0.02 | 0.0004 | 835984 | 2500.0 | 75.399 | 92.812 | 81.572 | 3.614 |
| 0.04 | 0.0016 | 208974 | 625.0 | 75.406 | 92.787 | 81.572 | 3.614 |
| 0.06 | 0.0036 | 92894 | 278.0 | 75.407 | 92.770 | 81.573 | 3.614 |
| 0.08 | 0.0064 | 52243 | 156.0 | 75.401 | 92.678 | 81.572 | 3.615 |
| 0.10 | 0.0100 | 33441 | 100.0 | 75.421 | 92.674 | 81.575 | 3.616 |
| 0.12 | 0.0144 | 23206 | 69.0 | 75.417 | 92.594 | 81.571 | 3.613 |
| 0.14 | 0.0196 | 17060 | 51.0 | 75.404 | 92.755 | 81.574 | 3.616 |
| 0.16 | 0.0256 | 13063 | 39.0 | 75.409 | 92.742 | 81.572 | 3.615 |
| 0.18 | 0.0324 | 10311 | 31.0 | 75.407 | 92.643 | 81.569 | 3.612 |
| 0.20 | 0.0400 | 8362 | 25.0 | 75.408 | 92.548 | 81.573 | 3.613 |
| 0.22 | 0.0484 | 6907 | 21.0 | 75.426 | 92.461 | 81.573 | 3.616 |
| 0.24 | 0.0576 | 5796 | 17.4 | 75.420 | 92.522 | 81.567 | 3.613 |
| 0.26 | 0.0676 | 4942 | 14.8 | 75.423 | 92.643 | 81.567 | 3.611 |
| 0.28 | 0.0784 | 4265 | 12.8 | 75.427 | 92.554 | 81.572 | 3.616 |
| 0.30 | 0.0900 | 3714 | 11.1 | 75.436 | 92.467 | 81.566 | 3.606 |
| 0.32 | 0.1024 | 3266 | 9.8 | 75.479 | 92.447 | 81.565 | 3.612 |
| 0.34 | 0.1156 | 2894 | 8.7 | 75.481 | 92.493 | 81.571 | 3.609 |
| 0.36 | 0.1296 | 2579 | 7.7 | 75.499 | 92.531 | 81.566 | 3.607 |
| 0.38 | 0.1444 | 2318 | 6.9 | 75.477 | 92.458 | 81.564 | 3.606 |
| 0.40 | 0.1600 | 2085 | 6.3 | 75.432 | 92.419 | 81.574 | 3.608 |
| 0.42 | 0.1764 | 1895 | 5.7 | 75.425 | 92.376 | 81.579 | 3.619 |
| 0.44 | 0.1936 | 1730 | 5.2 | 75.512 | 92.549 | 81.578 | 3.613 |
| 0.46 | 0.2116 | 1574 | 4.7 | 75.426 | 92.312 | 81.555 | 3.603 |
| 0.48 | 0.2304 | 1451 | 4.3 | 75.511 | 92.742 | 81.584 | 3.623 |
| 0.50 | 0.2500 | 1336 | 4.0 | 75.491 | 92.556 | 81.582 | 3.625 |
| 0.52 | 0.2704 | 1236 | 3.7 | 75.495 | 92.289 | 81.568 | 3.616 |
| 0.54 | 0.2916 | 1150 | 3.4 | 75.493 | 92.491 | 81.564 | 3.608 |
| 0.56 | 0.3136 | 1063 | 3.2 | 75.472 | 92.346 | 81.564 | 3.609 |
| 0.58 | 0.3364 | 996 | 3.0 | 75.566 | 92.354 | 81.565 | 3.612 |
| 0.60 | 0.3600 | 927 | 2.8 | 75.432 | 92.289 | 81.577 | 3.600 |
| 0.62 | 0.3844 | 869 | 2.6 | 75.483 | 92.159 | 81.570 | 3.606 |
| 0.64 | 0.4096 | 817 | 2.4 | 75.545 | 92.478 | 81.574 | 3.629 |
| 0.66 | 0.4356 | 766 | 2.3 | 75.542 | 92.333 | 81.595 | 3.630 |

Table A2. Elevation statistics of resampled DEMs from the terrestrial LIDAR survey on 02/08/2015

| Cell x,y (m) | Resolution ($m^2$) | Pts | Pts/$m^2$ | Min Z (m) | Max Z (m) | Mean Z (m) | Std Z (m) |
|---|---|---|---|---|---|---|---|
| 0.02 | 0.0004 | 836635 | 2500.0 | 75.384 | 92.817 | 81.584 | 3.600 |
| 0.04 | 0.0016 | 209180 | 625.0 | 75.396 | 92.795 | 81.584 | 3.601 |
| 0.06 | 0.0036 | 92966 | 278.0 | 75.392 | 92.767 | 81.583 | 3.600 |
| 0.08 | 0.0064 | 52304 | 156.0 | 75.404 | 92.766 | 81.585 | 3.601 |
| 0.10 | 0.0100 | 33469 | 100.0 | 75.407 | 92.697 | 81.585 | 3.601 |
| 0.12 | 0.0144 | 23241 | 69.0 | 75.407 | 92.635 | 81.583 | 3.599 |
| 0.14 | 0.0196 | 17074 | 51.0 | 75.411 | 92.732 | 81.585 | 3.601 |
| 0.16 | 0.0256 | 13069 | 39.0 | 75.408 | 92.675 | 81.585 | 3.600 |
| 0.18 | 0.0324 | 10322 | 31.0 | 75.409 | 92.524 | 81.582 | 3.595 |
| 0.20 | 0.0400 | 8366 | 25.0 | 75.411 | 92.748 | 81.585 | 3.604 |
| 0.22 | 0.0484 | 6914 | 21.0 | 75.438 | 92.608 | 81.589 | 3.603 |
| 0.24 | 0.0576 | 5812 | 17.4 | 75.404 | 92.743 | 81.583 | 3.601 |
| 0.26 | 0.0676 | 4948 | 14.8 | 75.402 | 92.549 | 81.583 | 3.597 |
| 0.28 | 0.0784 | 4272 | 12.8 | 75.451 | 92.408 | 81.590 | 3.604 |
| 0.30 | 0.0900 | 3719 | 11.1 | 75.457 | 92.642 | 81.588 | 3.608 |
| 0.32 | 0.1024 | 3267 | 9.8 | 75.464 | 92.568 | 81.578 | 3.599 |
| 0.34 | 0.1156 | 2898 | 8.7 | 75.437 | 92.430 | 81.591 | 3.609 |
| 0.36 | 0.1296 | 2586 | 7.7 | 75.421 | 92.635 | 81.584 | 3.602 |
| 0.38 | 0.1444 | 2323 | 6.9 | 75.510 | 92.563 | 81.588 | 3.607 |
| 0.40 | 0.1600 | 2092 | 6.3 | 75.483 | 92.520 | 81.588 | 3.601 |
| 0.42 | 0.1764 | 1896 | 5.7 | 75.496 | 92.524 | 81.575 | 3.594 |
| 0.44 | 0.1936 | 1731 | 5.2 | 75.493 | 92.318 | 81.582 | 3.606 |
| 0.46 | 0.2116 | 1580 | 4.7 | 75.417 | 92.422 | 81.585 | 3.600 |
| 0.48 | 0.2304 | 1456 | 4.3 | 75.515 | 92.418 | 81.594 | 3.608 |
| 0.50 | 0.2500 | 1340 | 4.0 | 75.427 | 92.697 | 81.593 | 3.601 |
| 0.52 | 0.2704 | 1237 | 3.7 | 75.509 | 92.344 | 81.584 | 3.610 |
| 0.54 | 0.2916 | 1151 | 3.4 | 75.443 | 92.398 | 81.585 | 3.593 |
| 0.56 | 0.3136 | 1070 | 3.2 | 75.492 | 92.522 | 81.575 | 3.605 |
| 0.58 | 0.3364 | 990 | 3.0 | 75.554 | 92.502 | 81.596 | 3.618 |
| 0.60 | 0.3600 | 930 | 2.8 | 75.459 | 92.402 | 81.616 | 3.621 |
| 0.62 | 0.3844 | 871 | 2.6 | 75.580 | 92.235 | 81.582 | 3.604 |
| 0.64 | 0.4096 | 814 | 2.4 | 75.563 | 91.934 | 81.580 | 3.578 |
| 0.66 | 0.4356 | 771 | 2.3 | 75.491 | 92.409 | 81.611 | 3.619 |

Table A3. Residual mean square error (MSE) for segmented regression fits at break points between 0.0100 $m^2$ (0.01 m x 0.01 m) resolution and 0.3136 $m^2$ (0.56 m x 0.56 m) resolution. Strongest fits indicated by the lowest MSE are in bold.

| Cell x,y (m) | Resolution ($m^2$) | Erosion MSE ($m^3$) | Deposition MSE ($m^3$) |
|---|---|---|---|
| 0.10 | 0.0100 | 0.2614 | 0.3229 |
| 0.12 | 0.0144 | 0.2521 | 0.3077 |
| 0.14 | 0.0196 | 0.2510 | 0.2965 |
| 0.16 | 0.0256 | 0.2493 | 0.2960 |
| 0.18 | 0.0324 | **0.2490** | 0.2953 |
| 0.20 | 0.0400 | 0.2492 | 0.2961 |
| 0.22 | 0.0484 | 0.2504 | 0.2963 |
| 0.24 | 0.0576 | 0.2539 | 0.2884 |
| 0.26 | 0.0676 | 0.2521 | 0.2631 |
| 0.28 | 0.0784 | 0.2538 | **0.2516** |
| 0.30 | 0.0900 | 0.2622 | 0.2601 |
| 0.32 | 0.1024 | 0.2665 | 0.2941 |
| 0.34 | 0.1156 | 0.2619 | 0.3097 |
| 0.36 | 0.1296 | 0.2720 | 0.3468 |
| 0.38 | 0.1444 | 0.2667 | 0.3685 |
| 0.40 | 0.1600 | 0.2778 | 0.3814 |
| 0.42 | 0.1764 | 0.2862 | 0.4004 |
| 0.44 | 0.1936 | 0.2928 | 0.4027 |
| 0.46 | 0.2116 | 0.2936 | 0.4088 |
| 0.48 | 0.2304 | 0.2902 | 0.4009 |
| 0.50 | 0.2500 | 0.2949 | 0.4198 |
| 0.52 | 0.2704 | 0.2946 | 0.4211 |
| 0.54 | 0.2916 | 0.2770 | 0.4032 |
| 0.56 | 0.3136 | 0.2882 | 0.4085 |

## Appendix II. Large photographs from the study site



Figure A1. Headwall material deposited in the gully channel




Figure A2. The photographs were taken near the base of the gully headwall on (a) 12/24/2014 and (b) 02/08/2015. A section of the pool drainage pipe is shown to have fallen and been buried by material from the headwall.

## Appendix III. R Segmented Regression

```
# jmcnelis@utk.edu
setwd("C:\\Users\\jmcne\\Documents\\R_THESIS\\SEGREG\\")
fl <- file("data.txt")
listdata <- read.table(fl, text="Element1\tElement2\tElement3", header=FALSE)
res <- listdata$V1
ero <- listdata$V2
dep <- listdata$V3

# List of break points to test iteratively
breaks <- res[which(res >= 0.10 & res <= 0.56)]
print(breaks)
        [1] 0.10 0.12 0.14 0.16 0.18 0.20 0.22 0.24 0.26 0.28 0.30 0.32 0.34 0.36 0.38 0.40 0.42 0.44 0.46
        [20] 0.48 0.50 0.52 0.54 0.56

# Loop through break points fitting segmented regression at each. Add residual mean square error of the
# points around each fit to variable MSE.
mse <- numeric(length(breaks))
for(i in 1:length(breaks)){
  piecewise1 <- lm(ero ~ res*(res < breaks[i]) + res*(res >= breaks[i]))
  mse[i] <- summary(piecewise1)[6]
}
mse <- as.numeric(mse)
print(mse)
        [1] 0.2614460 0.2520790 0.2509769 0.2493197 0.2489516 0.2491845 0.2504148 0.2539121 0.2521283
        [10] 0.2537838 0.2622016 0.2665324 0.2619074 0.2719859 0.2666546 0.2778436 0.2862343 0.2927546
        [19] 0.2935723 0.2901938 0.2948775 0.2946492 0.2769652 0.2882196
mse2 <- numeric(length(breaks))
for(i in 1:length(breaks)){
  piecewise2 <- lm(dep ~ res*(res < breaks[i]) + res*(res >= breaks[i]))
  mse2[i] <- summary(piecewise2)[6]
}
```

```
mse2 <- as.numeric(mse2)
print(mse2)
    [1] 0.3228827 0.3077458 0.2964695 0.2959319 0.2952986 0.2961189 0.2962717 0.2883851 0.2631150
    0.2515626 0.2630591
    [12] 0.2940951 0.3096801 0.3467952 0.3685264 0.3813617 0.4004167 0.4027332 0.4087712 0.4009226
    0.4197831 0.4210767
    [23] 0.4032393 0.4084569

# Determine lowest residual MSE. Plot residual MSE for each break point.
msemin <- breaks[which(mse==min(mse))]
plot(breaks,mse,xlab="Break points",ylab="mean squared error (m)",pch=16)
print(msemin)
    0.18
msemin2 <- breaks[which(mse2==min(mse2))]
plot(breaks,mse2,xlab="Break points",ylab="mean squared error (m)",pch=16)
print(msemin2)
    0.28

# Fit segmented regression to break point with lowest residual MSE.
piecewise1final <- lm(ero ~ res*(res < msemin) + res*(res > msemin))
summary(piecewise1final)
    Call:
    lm(formula = ero ~ res * (res < msemin) + res * (res > msemin))

    Residuals:
    Min      1Q  Median      3Q     Max
    -0.60358 -0.08962  0.01733  0.13594  0.48712

    Coefficients: (1 not defined because of singularities)
    Estimate Std. Error t value Pr(>|t|)
    (Intercept)         10.44187    0.26212  39.836  < 2e-16 ***
    res                 4.76739    0.37354  12.763 3.43e-13 ***
    res < mseminTRUE      1.00813    0.32814   3.072  0.00469 **
```

```
res > mseminTRUE     -0.01268    0.27492  -0.046  0.96354
res:res < mseminTRUE -6.01739    1.99000  -3.024  0.00530 **
res:res > mseminTRUE       NA         NA      NA       NA
---
Signif. codes:  0 ‘***’ 0.001 ‘**’ 0.01 ‘*’ 0.05 ‘.’ 0.1 ‘ ’ 1

Residual standard error: 0.2533 on 28 degrees of freedom
Multiple R-squared:  0.9139,           Adjusted R-squared:  0.9016
F-statistic:  74.3 on 4 and 28 DF,  p-value: 1.697e-14
```

```
piecewise2final <- lm(dep ~ res*(res < msemin2) + res*(res > msemin2))
summary(piecewise2final)
```

```
Call:
lm(formula = dep ~ res * (res < msemin2) + res * (res > msemin2))

Residuals:
     Min       1Q   Median       3Q      Max
-0.58070 -0.11923  0.01228  0.13846  0.53158

Coefficients: (1 not defined because of singularities)
                    Estimate Std. Error t value Pr(>|t|)
(Intercept)          12.1140     0.2857  42.406  < 2e-16 ***
res                   7.8070     0.5161  15.127 5.28e-15 ***
res < msemin2TRUE     1.2744     0.3204   3.978 0.000446 ***
res > msemin2TRUE     0.4070     0.2731   1.490 0.147289
res:res < msemin2TRUE  -6.8455     1.0490  -6.525 4.50e-07 ***
res:res > msemin2TRUE       NA         NA      NA       NA
---
Signif. codes:  0 ‘***’ 0.001 ‘**’ 0.01 ‘*’ 0.05 ‘.’ 0.1 ‘ ’ 1

Residual standard error: 0.2464 on 28 degrees of freedom
Multiple R-squared:  0.9772,    Adjusted R-squared:  0.9739
F-statistic: 299.9 on 4 and 28 DF,  p-value: < 2.2e-16
```

## Appendix IV. R test XYZ to array

```
> proct <- proc.time()
> xyz <- read.table("tls1_02.xyz")
> proc.time() – proct
user   system   elapsed
2.64   0.08   2.72
> proct <- proc.time()
> xyz <- read.table("tls1_28.xyz")
> proc.time() – proct
user   system   elapsed
0.04   0.00   0.03
> proct <- proc.time()
> xyz <- read.table("tls1001.xyz")
> proc.time() – proct
user   system   elapsed
99.28   1.69   103.00
```

# VITA

John McNelis was born in Memphis, TN, to the parents of JJ and Mary McNelis. He has a brother: Kevin. He attended St. Dominic School and Christian Brothers High School in Memphis, Tennessee. After graduation, he moved to Knoxville, Tennessee to attend the University of Tennessee. He majored in an interdisciplinary program for Environmental Studies, which he completed in four years to attain his Bachelor of Arts degree in December of 2012. He began the graduate program in the Department of Geography at the University of Tennessee in Fall 2013 and completed the program with a Masters of Science degree in Geography in May 2016.